# Phase transitions in $N = 40$, 60, and 90 nuclei

A. Prášek* and P. Alexa
*Department of Physics, VŠB–Technical University Ostrava, 17. listopadu 2172/15, CZ-708 00 Ostrava, Czech Republic*

D. Bonatsos
*Institute of Nuclear and Particle Physics, National Centre of Scientific Research Demokritos, GR-15310 Aghia Paraskevi, Attiki, Greece*

G. Thiamová
*Université Grenoble 1, CNRS, LPSC, Institut Polytechnique de Grenoble, IN2P3, F-38026 Grenoble, France*

D. Petrellis and P. Veselý
*Nuclear Physics Institute, Czech Academy of Sciences, CZ-250 68 Řež near Prague, Czech Republic*

(Received 20 April 2024; accepted 9 July 2024; published 20 August 2024)

In this paper we focus on three mass regions where first-order phase transitions occur, namely, for $N = 40$, 60, and 90. We investigate four isotopic chains (Se, Zr, Mo, and Nd) in the framework of microscopic Skyrme-Hartree-Fock+Bardeen-Cooper-Schrieffer calculations for 15 different parametrizations. The microscopic calculations show the typical behavior expected for first-order phase transitions. To find the best candidate for the critical point phase transition we propose different microscopic position and occupation indices calculated for positive-parity and negative-parity proton and neutron single-quasiparticle states around the Fermi level. The microscopic calculations are completed by macroscopic calculations within the algebraic collective model (ACM), and compared with the experimental data for $^{74}$Se, $^{102}$Mo, and $^{150}$Nd, considered to be the best candidates for the critical-point nuclei.

DOI: 10.1103/PhysRevC.110.024317

## I. INTRODUCTION

Quantum phase transitions (QPTs) [1–3] and critical-point symmetries (CPSs) [4–7] in even-even atomic nuclei belong to one of most studied topics in nuclear structure physics for several decades. They are observed in chains of isotopes in which the addition of two neutrons causes a radical change of the nuclear structure, the sudden jump from vibrational behavior in $^{150}$Sm to rotational behavior in $^{152}$Sm [5,8] being a characteristic example. The neutron number is used as a control parameter in these transitions [9], while various collective quantities are used as the order parameter [10–13].

The Ehrenfest classification of nuclear QPTs started in 1981 [14], with the realization that, within the parameter space of the interacting boson model [15–18], a second-order QPT takes place between U(5) (spherical) [15] and O(6) ($\gamma$ unstable, i.e., soft towards triaxial deformation) [17] nuclei, while a first-order QPT occurs between U(5) (spherical) and SU(3) (deformed) [16] nuclei. The critical-point symmetries E(5) [4,19] and X(5) [5,20,21] have been introduced in 2000 and 2001, respectively, for the description of these QPTs within the framework of the Bohr collective Hamiltonian [22–24] providing parameter independent (up to overall scales) predictions for spectra and transition rates at the critical point of these QPTs. The $N = 90$ isotones $^{150}$Nd [25], $^{152}$Sm [8], $^{154}$Gd [26], $^{156}$Dy [27] have been suggested as the best experimental manifestations of the X(5) CPS. A $\gamma$-rigid version of X(5), called X(3), in which the $\gamma$ value has been fixed to zero, has also been introduced [28].

Even before the introduction of the concept of CPS, the mechanism of the onset of deformation within microscopic models was investigated in a series of papers by Federman and Pittel [29–32]. They pointed out the crucial role played by the proton-neutron interaction in the creation of deformation, in particular stressing the major role played by intruder neutron orbitals in the development of deformation across the nuclear chart. In addition, the concept of quasi-dynamical symmetries [33], i.e., symmetries persisting in the presence of strong symmetry-breaking interactions has been introduced for both first-order [34] and second-order [35,36] QPTs.

Recently, the connection between CPSs linked to QPTs and the effect of shape coexistence (SC) [37–41] attracted considerable interest [42–45]. Shape coexistence [37–41] is said to occur in nuclei in which the ground-state band and an excited $K = 0$ band lie close in energy and simultaneously exhibit radically different structures and symmetries; for example, one of them being spherical and the other one deformed, or both of them being deformed, but one of them exhibiting a prolate (rugby-ball-like) shape and the other one showing an oblate (pancake-like) one. The $N = 60$ isotones $^{100}$Zr [42–44] and $^{98}$Sr [45] have been found as the best nuclei

*Deceased.

 

in which the connection between CPS and QPT is observed. The relevant studies have been carried out in the framework of the IBM with configuration mixing (IBM-CM), which takes particle-hole (p-h) excitations into account [46–49] and allows for mixing of the ground-state configuration of $N$ bosons with the excited 2p-2h configuration, described by $N+2$ bosons [50,51]. It should be noticed that the occurrence of phase coexistence in the region of transition between spherical and deformed shapes has been pointed out in the IBM framework already in 1998 [52], while the structural similarity between the $N=90$ and $N=60$ regions has been pointed out already in 1981 [53], implying a common microscopic origin of the QPT from spherical to deformed shapes in these two regions. Furthermore, it has been recently suggested [54–56] that $^{100}$Zr is the critical point of two intertwined QPTs, the one from spherical to deformed shapes already mentioned and another one from normal configurations (without particle-hole excitations) to intruder configurations (involving particle-hole excitations).

In addition, a recent study [57] of the systematics of energy levels and $B(E2)$ transition rates in the $N=40$ region around $^{74}$Se pointed out the structural similarity of the $N=40$ region to the above-mentioned $N=60$ and $N=90$ regions. It has been shown that in all these three regions intruder orbitals start participating to the onset of deformation. In particular, neutron particle-hole excitations are found to lead to both SC and QPT from spherical to prolate deformed shapes taking place in parallel.

The above findings suggest that the three regions with $N=90$, $N=60$, and $N=40$ exhibit in a similar way a QPT from spherical to deformed shapes, based on the microscopic picture of the onset of deformation due to increased proton-neutron interaction, with SC triggered at the same time by the creation of neutron particle-hole excitations [called proton-induced particle-hole excitations in the framework of the dual shell mechanism [58] for SC developed within the proxy-SU(3) approximation [59–61], corroborated through covariant density-functional theory calculations [62,63]]. Theoretical calculations in these three regions, related to the presence of SC, have been recently reviewed in Ref. [41].

However, despite the similar microscopic origins of the three regions, only the critical isotones with $N=90$ can be described in terms of the parameter-free predictions of the X(5) CPS [8,25–27], while for $N=60$ and $N=40$ the data for spectra and $B(E2)$ transition rates are far from the X(5) predictions. It is therefore of interest to look for a more flexible theoretical framework, possibly able to accommodate these three critical regions simultaneously.

Therefore, in the present paper we investigate the three CPS regions within different microscopic and macroscopic approaches, attempting to shed more light on the nature of the CPS and possibly find a common framework for all of them. In Sec. II empirical systematics of different spectral and transitional signatures of CPS are discussed in the three regions of interest. In Sec. III we turn to microscopic calculations based on the Skyrme-Hartree-Fock+Bardeen-Cooper-Schrieffer (SHF+BCS) model to study potential-energy curves (PECs) as functions of quadrupole, octupole and hexadecapole deformations, and introduce microscopic position and occupation indices for positive-parity and negative-parity proton and neutron single-quasiparticle states around the Fermi level. In Sec. IV we briefly introduce the algebraic collective model (ACM), which is then applied to $^{74}$Se, $^{102}$Mo, and $^{150}$Nd in Sec. V.

## II. EMPIRICAL SYSTEMATICS

We are going to use the energy ratios

$$R_{4/2}=\frac{E(4_1^+)}{E(2_1^+)},\quad R_{2/0}=\frac{E(2_1^+)}{E(0_2^+)},\quad R_{2/2}=\frac{E(2_\gamma^+)}{E(2_1^+)},\tag{1}$$

as well as the rates of change with the neutron number $N$ (which possess twice the value of relevant mathematical derivative),

$$\begin{aligned}\frac{\mathrm{d}R_{4/2}}{\mathrm{d}N}(N)&=R_{4/2}(N)-R_{4/2}(N-2),\\ \frac{\mathrm{d}R_{2/2}}{\mathrm{d}N}(N)&=R_{2/2}(N)-R_{2/2}(N-2).\end{aligned}\tag{2}$$

In addition we are going to use the transition rates $B(E2;2_1^+\to 0_1^+)$, and their rate of change with the neutron number $N$ (which possesses twice the value of relevant mathematical derivative),

$$\begin{aligned}\frac{\mathrm{d}B(E2;2_1^+\to 0_1^+)}{\mathrm{d}N}(N)&=B(E2;2_1^+\to 0_1^+)(N)\\ &\quad-B(E2;2_1^+\to 0_1^+)(N-2),\end{aligned}\tag{3}$$

The ratio $R_{4/2}$ is a well-known indicator of collectivity [64], obtaining values 2.0–2.4 for near-spherical nuclei, 2.4–3.0 for $\gamma$-unstable nuclei, and 3.0–3.33 for deformed nuclei.

The transition rate $B(E2;2_1^+\to 0_1^+)$ is known [65] to be proportional to the square of the quadrupole deformation parameter $\beta$, expressing the deviation of the nuclear shape from sphericity.

The ratio $R_{2/0}$ is known [57] to exhibit a maximum in the region of the QPT from spherical to deformed nuclei.

In Fig. 1 an abrupt increase of $R_{4/2}$ is seen at $N=90$ in the Nd-Sm-Gd-Dy region, at $N=60$ in the Sr-Zr-Mo region, and at $N=42$ in the Zn-Ge-Se region. This is corroborated by the rate of change of $R_{4/2}$ vs $N$ [10] within these series of isotopes.

In Fig. 2 an abrupt increase of $B(E2;2_1^+\to 0_1^+)$ is seen around $N=90$ in the Nd-Sm-Gd-Dy region, around $N=60$ in the Sr-Zr-Mo region, and around $N=42$ in the Zn-Ge-Se region. This is corroborated by the rate of change of $B(E2;2_1^+\to 0_1^+)$ vs $N$ [10] within these series of isotopes.

In Fig. 3 maxima of the energy ratio $R_{2/0}$ are seen around $N=88$ in the Nd-Sm-Gd-Dy region, around $N=58$ in the Sr-Zr-Mo region, and around $N=40$ in the Zn-Ge-Se region. In other words, the maxima appear two neutrons earlier in relation to the maximal changes of $R_{4/2}$ and $B(E2;2_1^+\to 0_1^+)$ seen in Figs. 1 and 2.

In Fig. 4 an abrupt increase of $R_{2/2}$ is seen around $N=90$ in the Nd-Sm-Gd-Dy region, around $N=60$ in the Sr-Zr-Mo

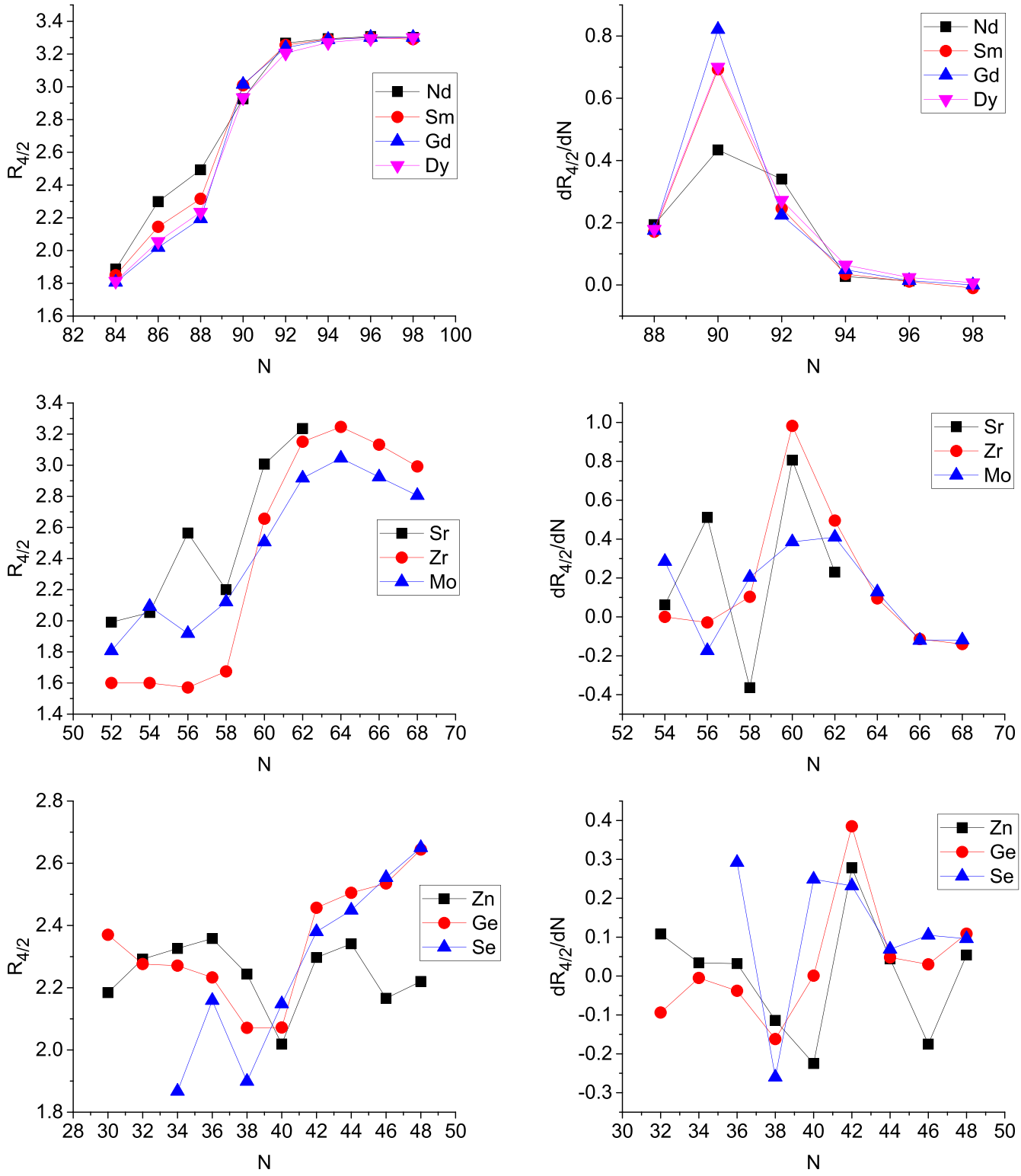


FIG. 1. Experimental [67] energy ratios $R_{4/2}$ and their rate of change $\mathrm{d}R_{4/2}/\mathrm{d}N$ with respect to the neutron number $N$ in the $N = 90$, 60, 40 regions. See Sec. II for further discussion.

region, and around $N = 42$ in the Zn-Ge-Se region. This is corroborated by the rate of change of $R_{2/2}$ vs $N$ [10] within these series of isotopes.

In Table I the values of these quantities for the nuclei close to the maxima are reported. We see that while the three regions exhibit in Figs. 1–4 very similar behavior, the numerical values in each region differ. In particular,

(a) the $R_{4/2}$ ratio exhibits near-rotational values in the $N = 90$ region, intermediate values in the $N = 60$ region,

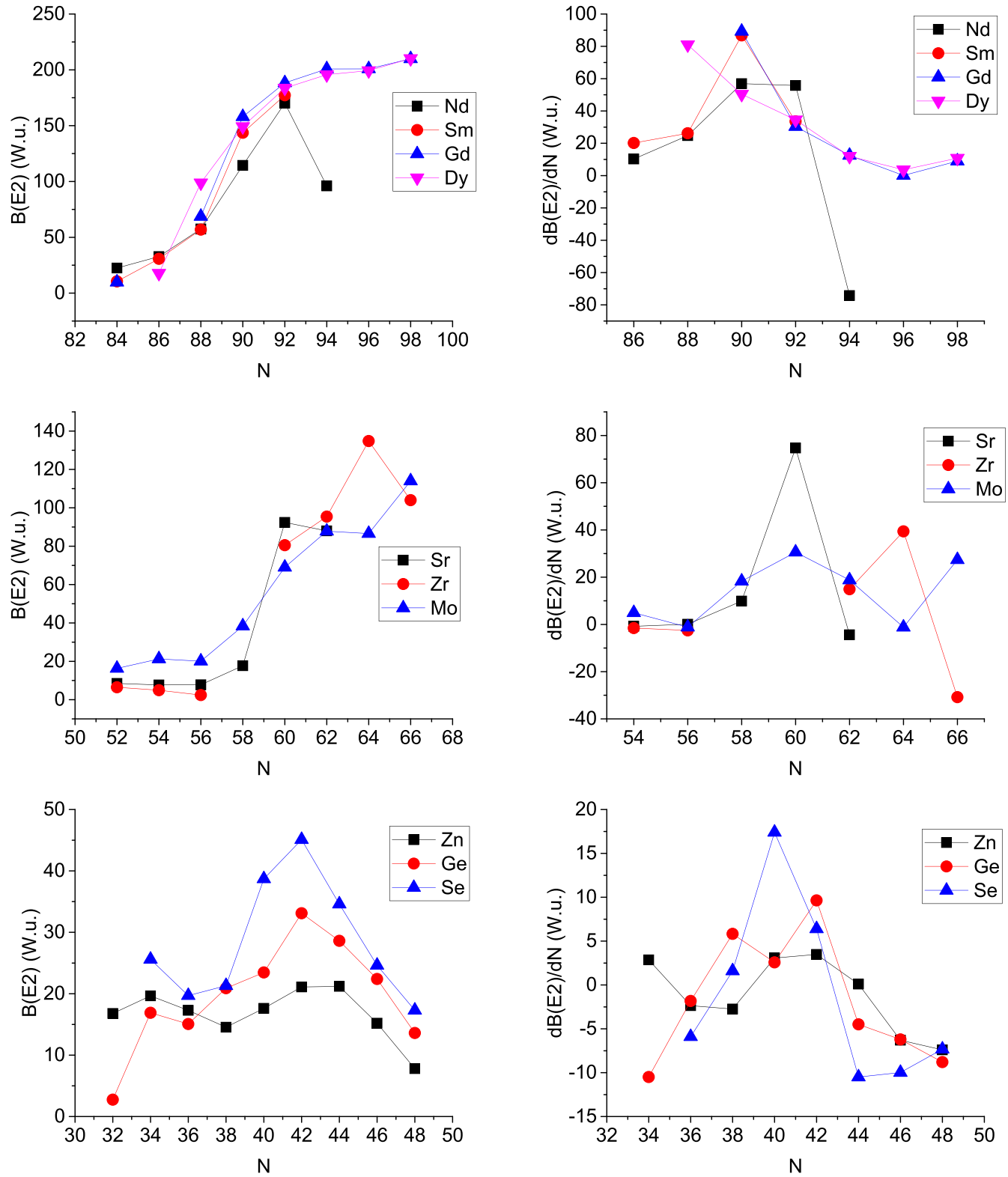


FIG. 2. Experimental $B(E2;2_1^+ \to 0_1^+)$ transition rates [68] and their rate of change $\mathrm{d}B(E2;2_1^+ \to 0_1^+)/\mathrm{d}N$ with respect to the neutron number $N$ in the $N = 90$, 60, 40 regions. See Sec. II for further discussion.

and much lower, near-vibrational values in the $N = 40$ region.

(b) in qualitative agreement with (a), the $B(E2;2_1^+ \to 0_1^+)$ transition rate exhibits higher values in the $N = 90$ region, intermediate values in the $N = 60$ region, and lower values in the $N = 40$ region. This is expected, since the $B(E2;2_1^+ \to 0_1^+)$ transition rate is proportional to the square of the quadrupole deformation

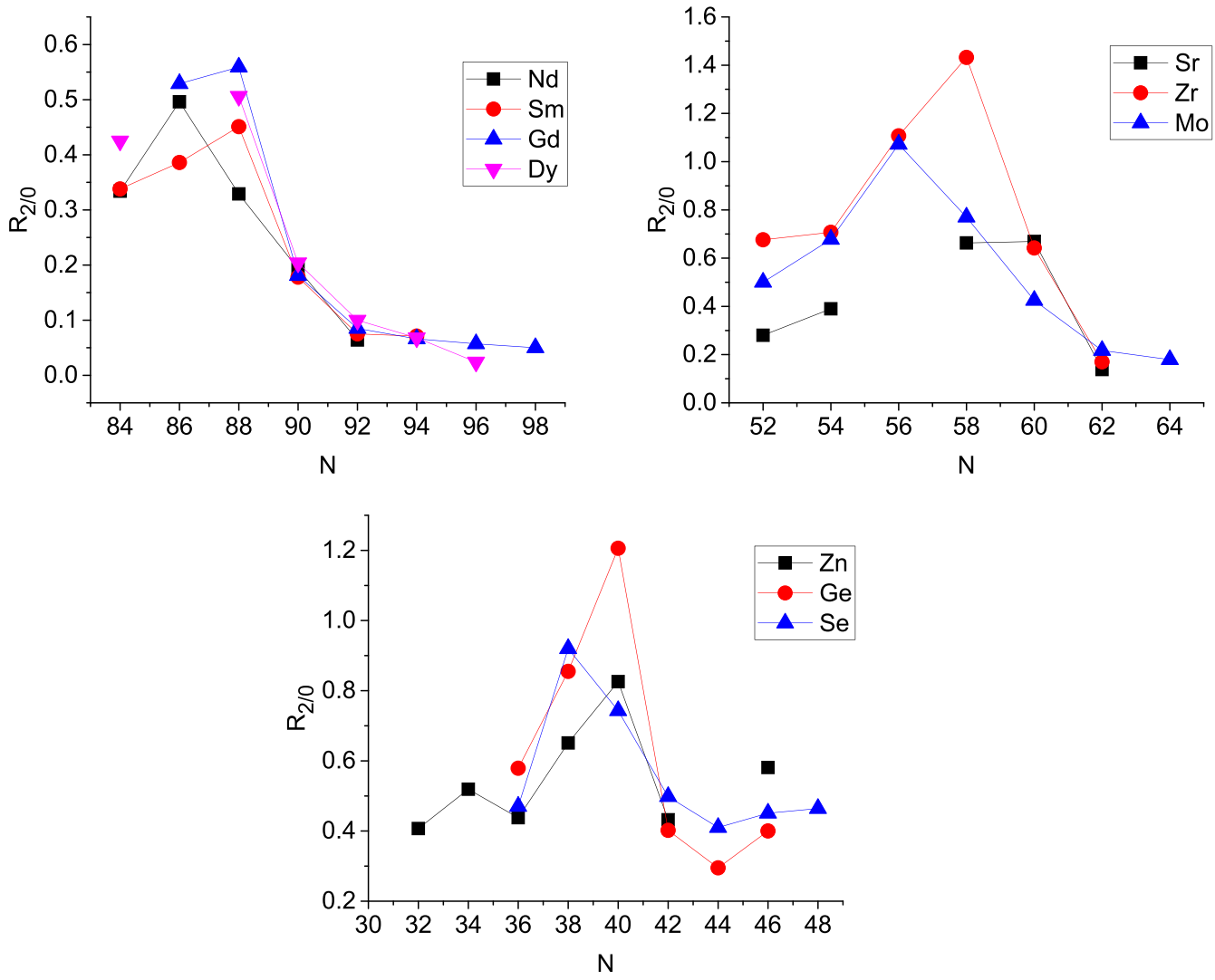


FIG. 3. Experimental [67] energy ratios $R_{2/0}$ in the $N = 90$, 60, 40 regions. See Sec. II for further discussion.

$\beta$ [65], despite the fact that part of the difference is due to the factor $A^{4/3}$ accompanying $\beta^2$ in the relevant equation [65].

(c) the $R_{2/0}$ values exhibit the opposite trend, namely, lower values in the $N = 90$ region, evolving to higher values in the $N = 40$ region, in agreement to the well-known fact [67] that the $0_2^+$ state raises to very high values as a nucleus approaches the rotational limit of $R_{4/2} = 10/3$.

(d) the $R_{2/2}$ ratio exhibits higher values in the $N = 90$ region, intermediate values in the $N = 60$ region, and lower values in the $N = 40$ region, corroborating the structural similarity between the ground state band and the $\gamma$ band [69].

These observations indicate that the parameter-independent values of $R_{4/2} = 2.904$ and $R_{2/0} = 0.177$ [5,66] characterizing the X(5) critical-point symmetry [5] apply very well to the $N = 90$ isotones, but they do not apply in the $N = 60$ and $N = 40$ regions, for which a more flexible model appears to be required. The values seen in the $N = 40$ region, in particular, are quite similar to the parameter-independent values of $R_{4/2} = 2.44$ and $R_{2/0} = 0.35$ seen in X(3) [70], the $\gamma$-rigid analog of X(5).

The $N = 90$ isotones $^{150}$Nd [25], $^{152}$Sm [8], $^{154}$Gd [26], $^{156}$Dy [27] are well established examples of the X(5) critical-point symmetry.

In the $N = 60$ region, $^{104}$Mo$_{62}$ has initially been suggested [71] as an X(5) candidate, based on its ratio $R_{4/2} = 2.917$, which is very close to the X(5) value of 2.904. In addition, its ratio $R_{2/0} = 0.217$, is also very close to the X(5) value of 0.177. However, it was later disregarded, since its $B(E2)$s within the ground-state band have been found [72] to exhibit a deformed behavior. Figures 1–4 suggest that the $N = 60$ isotones $^{98}$Sr, $^{100}$Zr, $^{102}$Mo are better candidates for the critical point of the spherical to deformed QPT in the $Z = 40$ region.

It should be noticed that Figs. 1–4 shed light on the nature of ground-state QPTs [3,11,12]. According to the Ehrenfest classification, a first-order phase transition occurs when the first derivative of a physical quantity (serving as the order parameter) exhibits a discontinuity with respect to the con-

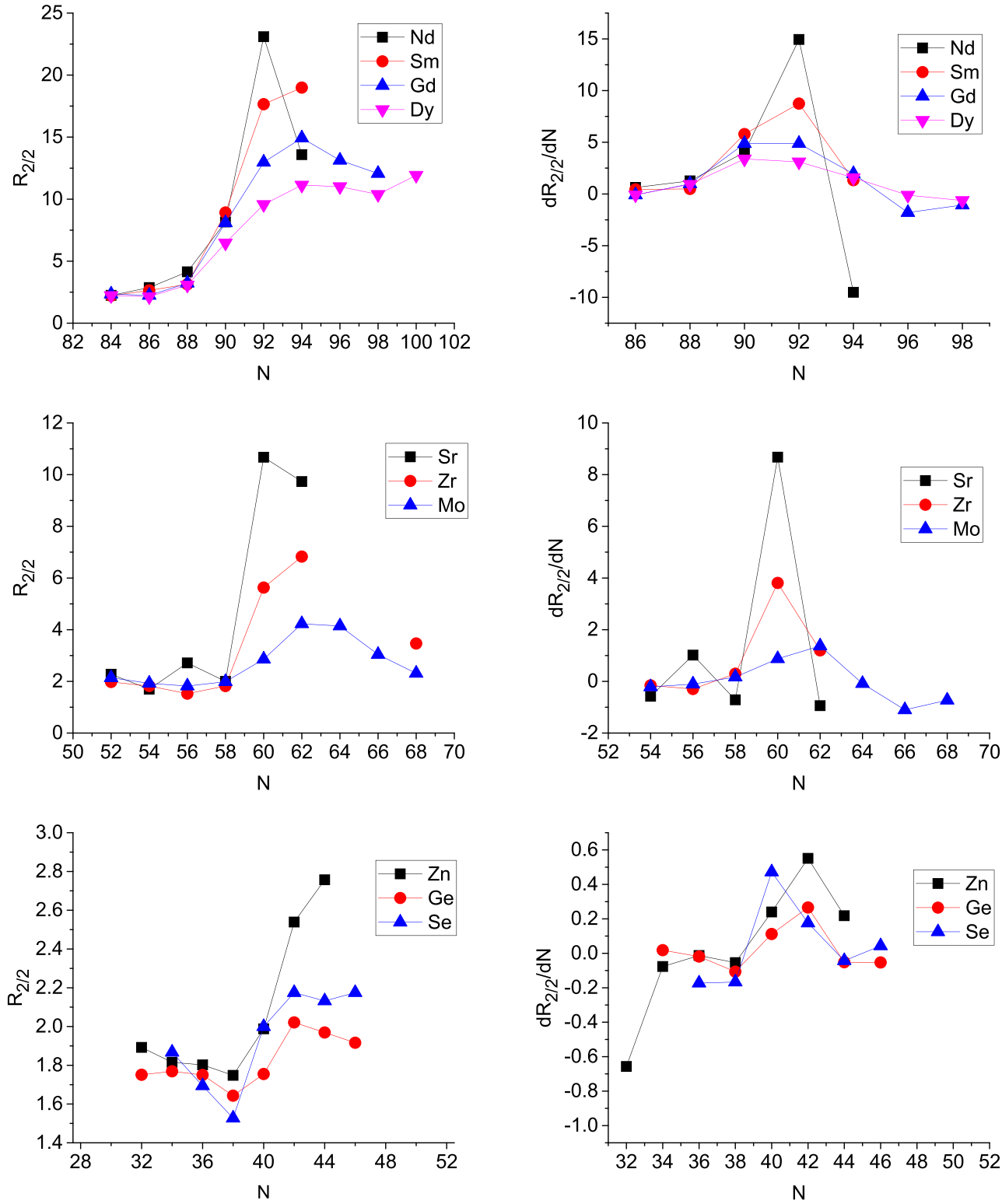


FIG. 4. Experimental [67] energy ratios $R_{2/2}$ and their rate of change $\mathrm{d}R_{2/2}/\mathrm{d}N$ with respect to the neutron number $N$ in the $N = 90$, 60, 40 regions. See Sec. II for further discussion.

trol parameter [11,12]. The ground-state spectra and $B(E2)$ transition rates shown in Figs. 1 and 2 suggest the occurrence of a first-order ground-state QPT within the ground-state band for nuclei around $N = 90$, 60, 42, since the rate of change of these quantities vs the neutron number $N$ exhibits a discontinuity, while the quantities themselves show an increase with $N$, which becomes abrupt at the critical point of the QPT. The same behavior is seen in Fig. 4, suggesting a similar behavior for the $\gamma$ band. However, this is not the case for the ratio $R_{2/0}$ (Fig. 3), which presents itself a maximum

TABLE I. Energy ratios $R_{4/2}$, $R_{2/2}$, and transition rates $B(E2; 2_1^+ \to 0_1^+)$, as well as their rates of change as a function of the neutron number $N$, $(dR_{4/2}/dN)(N)$, $(dR_{2/2}/dN)(N)$, and $[dB(E2)/dN](N)$, are listed for nuclei at $N = 90$, 60, 42, and 40, lying near the maxima appearing in Figs. 1–4. In addition, the energy ratios $R_{2/0}$ are shown for the isotones listed, labeled as $R_{2/0}(N)$. The parameter-independent predictions of the critical-point symmetries X(5) [5,66] and X(3) [28] are also shown for comparison. See Sec. II for further discussion.

| Nuc. | $R_{4/2}$ | $\frac{dR_{4/2}}{dN}(N)$ | $B(E2)$ W.u. | $\frac{dB(E2)}{dN}(N)$ W.u. | $R_{2/0}(N)$ | $R_{2/2}$ | $\frac{dR_{2/2}}{dN}(N)$ |
|---|---|---|---|---|---|---|---|
| $^{150}Nd_{90}$ | 2.927 | 0.434 | 114.4 | 56.9 | 0.193 | 8.156 | 4.017 |
| $^{152}Sm_{90}$ | 3.009 | 0.693 | 143.7 | 86.8 | 0.178 | 8.916 | 5.786 |
| $^{154}Gd_{90}$ | 3.015 | 0.821 | 158.0 | 89.3 | 0.181 | 8.095 | 4.873 |
| $^{156}Dy_{90}$ | 2.934 | 0.700 | 149.2 | 50.4 | 0.204 | 6.464 | 3.392 |
| $^{98}Sr_{60}$ | 3.006 | 0.806 | 92.4 | 74.7 | 0.669 | 10.674 | 8.676 |
| $^{100}Zr_{60}$ | 2.656 | 0.982 | 80.5 | | 0.642 | 5.628 | 3.808 |
| $^{102}Mo_{60}$ | 2.507 | 0.386 | 69.0 | 30.6 | 0.425 | 2.859 | 0.873 |
| $^{72}Zn_{42}$ | 2.297 | 0.278 | 21.1 | 3.5 | 0.432 | 2.539 | 0.551 |
| $^{74}Ge_{42}$ | 2.457 | 0.385 | 33.1 | 9.6 | 0.402 | 2.021 | 0.266 |
| $^{76}Se_{42}$ | 2.380 | 0.232 | 45.1 | 6.4 | 0.498 | 2.175 | 0.176 |
| $^{74}Se_{40}$ | 2.148 | 0.249 | 38.7 | 17.4 | 0.743 | 1.999 | 0.472 |
| X(5) | 2.907 | | | | 0.177 | | |
| X(3) | 2.440 | | | | 0.350 | | |

around the critical point. This difference is rooted to the fact that the ground-state band and the $\gamma$ band tend to have similar structures [69], while the nature of the $\beta$ band has been a point of controversy [73–76], with the first excited $0^+$ state being able to correspond to several different physical situations and not necessarily to the bandhead of the $\beta$ band [77].

## III. MICROSCOPIC MEAN-FIELD CALCULATIONS

The regions of interest have been investigated within several different mean-field frameworks. Nonrelativistic calculations using the Skyrme interaction have been performed for the Nd-Sm-Gd-Dy [78] and Zr [79,80] isotopes, while the Gogny interaction has been used in the Nd-Sm-Gd-Dy [81–83], Zr [84], and Se [85] regions. Relativistic mean-field calculations have been performed for the Nd-Sm-Gd-Dy [86–88] and Sr-Zr-Mo [89–92] isotopes. A five-dimensional quadrupole collective Hamiltonian with parameters determined from relativistic mean-field calculations has been used in the Nd-Sm-Gd-Dy [93–95] and Sr-Zr-Mo [96] isotopes. In addition, an IBM Hamiltonian with parameters determined by covariant density-functional theory calculations has been applied to the Nd-Sm-Gd-Dy [97–100], Sr-Zr-Mo [101], and Se [102] regions.

In the present section we are trying to accommodate all three regions of $N = 90$, $N = 60$, and $N = 40$ within the same theoretical framework.

Self-consistent mean-field methods based, e.g., on the most widely used Skyrme-Hartree-Fock+Bardeen-Cooper-Schrieffer (SHF+BCS) calculations [103] represent a microscopic possibility to investigate phase transitions in finite nuclei. One would expect to observe a typical bump structure in the potential-energy curve (PEC) calculations as a function

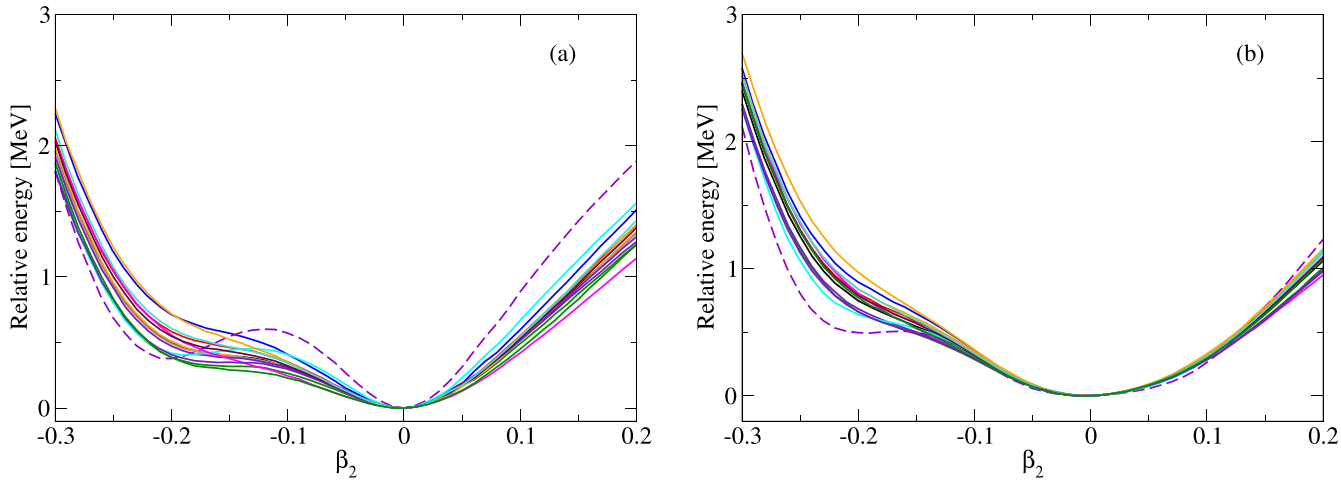


FIG. 5. PECs as a function of $\beta_2$ for (a) $^{74}$Se and (b) $^{76}$Se for all investigated parametrizations. The parametrization SV-mas07 (violet dashed) gives a slightly different PEC compared with the others.

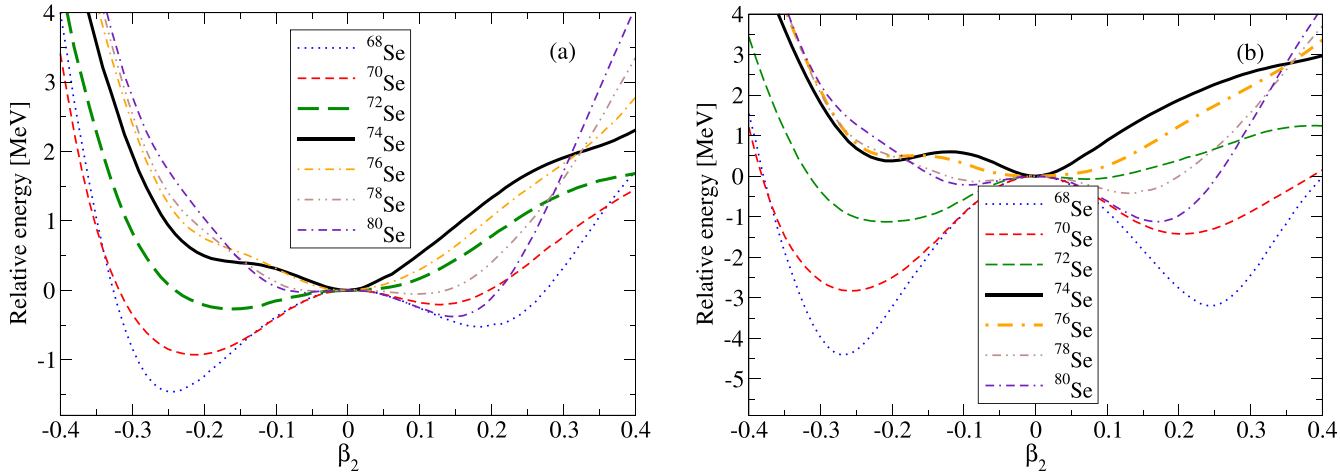


FIG. 6. PECs as a function of $\beta_2$ for the selenium isotopes for two SHF parametrizations, (a) SV-bas and (b) SV-mas07. Flat-bottomed PECs are indicated by thicker curves.

of the quadrupole deformation parameter $\beta_2$ [97,98], which manifests itself in a wider flat region around the minimum of the PEC compared with neighboring nuclei. In addition, the presence of opposite-parity intruder states in both proton and neutron single-quasiparticle spectra close to the Fermi level represents another microscopic signature of the phase transition [29–32].

Because there exist plenty of SHF functional parametrizations we investigate here the whole family of parametrizations based on the SV-bas one (15 parametrizations) [104]. In calculations using the axial SHF code SKYAX [105] with a density dependent $\delta$-force interaction in the pairing channel [106], single-particle levels up to 75 MeV were taken into account (eight oscillator shells). We investigated PECs as a function of quadrupole $\beta_2$, octupole $\beta_3$ and hexadecapole $\beta_4$ deformations for four isotopic chains around $N = 40$, 60, and 90 ($^{68}$Se–$^{80}$Se, $^{92}$Zr–$^{104}$Zr, $^{94}$Mo–$^{106}$Mo, $^{144}$Nd–$^{156}$Nd).

In the selenium chain all parametrizations predict similar PECs; the parametrization SV-mas07 gives slightly different results (see Fig. 5). In the quadrupole deformation PECs one observes phase transition from oblate to prolate shape at $N = 38$–44 (see Fig. 6). For $N = 40$ SC is predicted with one spherical and one oblate minimum close in energy. A wider flat region is observed for $N = 38$ and 40 (SV-bas) and for $N = 40$ and 42 (SV-mas07). Octupole deformation does not play any significant role, as expected. Hexadecapole deformation remains positive and close to zero ($\beta_4 = 0$ for $N = 40$ and 42).

In the zirconium chain all parametrizations again predict similar quadrupole-deformation PECs with a more pronounced minima for the SV-tls parametrization (see Figs. 7 and 8). Interestingly, for the SV-bas, one observes three minima: oblate, spherical, and prolate for $N \geqslant 58$, the oblate one and the spherical one being almost degenerate for $N = 60$ (the flattest PEC). For SV-tls, the flat-bottomed PECs were found for $N = 58$–60. Octupole deformation is again not important. Hexadecapole deformation is around $\beta_4 = 0$.

The molybdenum chain behaves similarly (see Figs. 9 and 10). The flat-bottomed PECs were found for $N = 60$ (SV-bas) and $N = 58$ (SV-tls).

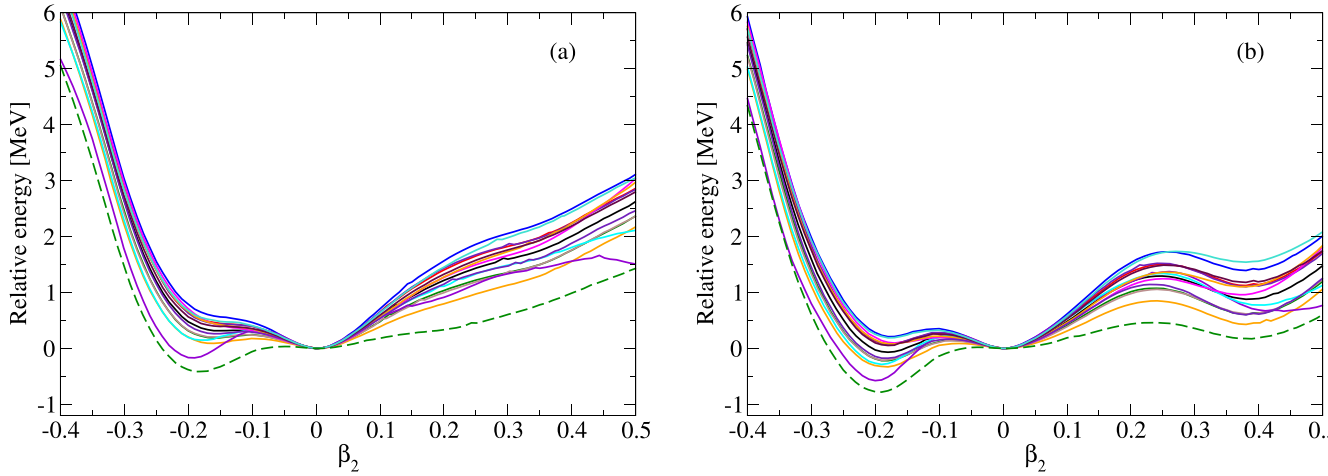


FIG. 7. PEC as a function of $\beta_2$ for (a) $^{98}$Zr and (b) $^{100}$Zr for all investigated parametrizations. The parametrization SV-tls (dark green dashed) gives a more pronounced oblate minimum and the lowest energy differences for different $\beta_2$ values.

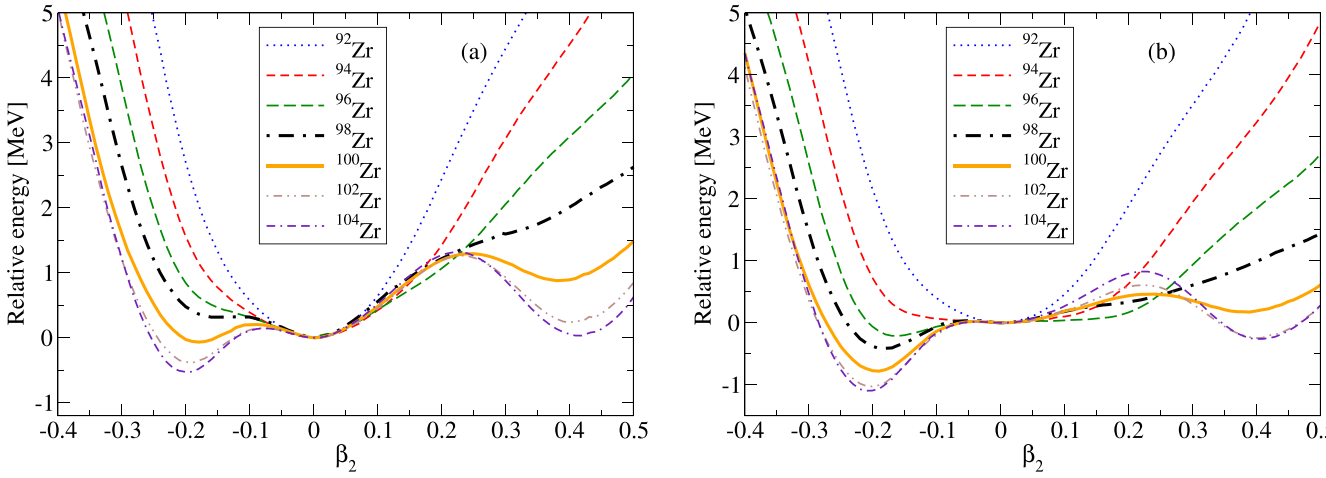


FIG. 8. PEC as a function of $\beta_2$ for the zirconium isotopes for two SHF parametrizations: (a) SV-bas and (b) SV-tls. Flat-bottomed PECs are indicated by thicker curves.

In the neodymium chain one observes a gradual development of prolate deformation (see Fig. 11) with a wider flat region around the prolate quadrupole deformation minimum for $N = 90$ for all parametrizations (see Fig. 12). Octupole deformation does not play any significant role; in the region $N \leqslant 90$ octupole deformation softness occurs. Hexadecapole deformation increases from $\beta_4 = 0$ to $\beta_4 = 0.22$ along the chain with a PEC wider flat region for $N = 60$ (see Fig. 13).

To check if triaxiality plays an important role in the investigated regions we have to use SKY3D code [107]. Results for the parametrization SV-bas are presented in Table II. Because the codes use different definitions of $\beta_2$, $\beta_{2\text{SKYAX}}$ is recalculated according to the $\beta_2$ definition in the SKY3D code. One can see that both values of $\beta_2$ coincide and the triaxiality is not important in the investigated regions.

To track the phase transitions on a single-quasiparticle level, one has to investigate a relative position of single-quasiparticle positive- and negative-parity proton and neutron states with respect to the Fermi level. We, therefore, define four new position indices $I(\nu, \pi)$ for proton positive-parity ($\nu = p$, $\pi = +$), proton negative-parity ($\nu = p$, $\pi = -$), neutron positive-parity ($\nu = n, \pi = +$), and neutron negative-parity ($\nu = n, \pi = -$) states. Values of $I(\nu, \pi)$ are found from $I(\nu, \pi) = \sum_{i(\nu,\pi)}(0.5 - |v_i^2 - 0.5|)$, where $v_i^2$ is the pairing occupation probability of the state $i$ and we sum over all model states of defined $\nu$ and $\pi$. Because $v^2 = 0.5$ exactly at the Fermi level, the contribution of the levels close to the Fermi level to the position index approaches the maximum value of 0.5, whereas the contribution of the levels far from the Fermi level approaches to zero. The position index also depends on the strength of the pairing force. If it is low, the indices approach zero, too. In the limit of zero pairing $v_i^2 = 0$ or 1 for all states $i$ and $I(\nu, \pi) = 0$. Parity enables the separation of intruder states: In the selenium isotopes ($Z = 34$) both proton and neutron intruder states have positive parity, while in the zirconium ($Z = 40$) and molybdenum ($Z = 42$) isotopes proton intruder states have positive parity and neutron intruder states have negative parity. In the neodymium

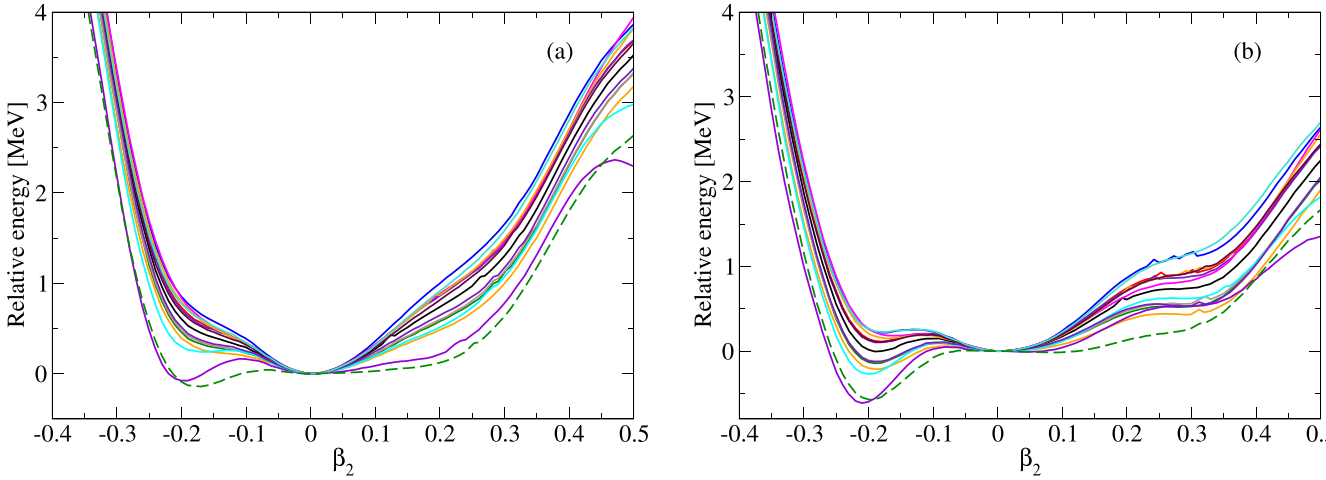


FIG. 9. PECs as a function of $\beta_2$ for (a) $^{100}$Mo and (b) $^{102}$Mo (b) for all investigated parametrizations. The parametrization SV-tls (dark green dashed) gives a more pronounced oblate minimum and the lowest energy differences for different $\beta_2$ values.

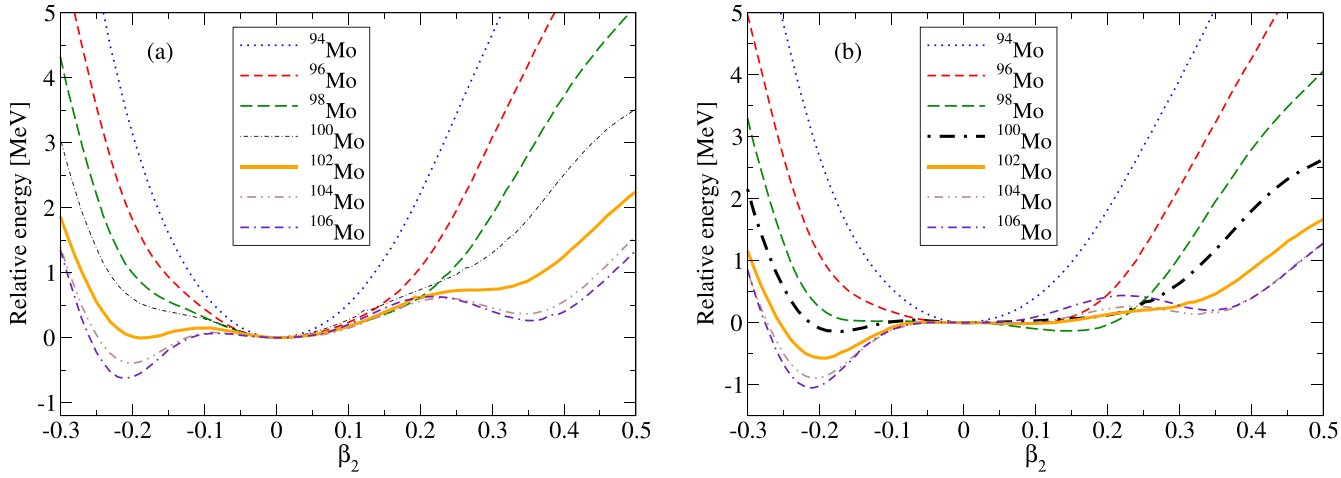


FIG. 10. PECs as a function of $\beta_2$ for the molybdenum isotopes for two SHF parametrizations: (a) SV-bas and (b) SV-tls. Flat-bottomed PECs are indicated by thicker curves.

($Z = 60$) isotopes, instead, proton intruder states have negative parity and neutron intruder states have positive parity. Results for selenium, zirconium, molybdenum, and neodymium chains are presented in Figs. 14 and 15 for the SV-bas parametrization.

In selenium isotopes protons and neutrons occupy the same shell and $I(p,+) = I(n,+)$ between $N = 38$ and 40 and around $N = 44$. $I(p,-) = I(n,-)$ symmetrically around $N = 40$ for $N = 36$ and $N = 44$. In zirconium isotopes $I(p,-) = I(n,-)$ for $N = 56$ and neutron intruder position index $I(n,-)$ reaches its maximum for $N = 60$, i.e., these states are closer to the Fermi level. In molybdenum isotopes $I(p,-) = I(n,-)$ again close to $N = 56$ and the neutron intruder position index $I(n,-)$ gradually increases up to $N = 60$.

In neodymium isotopes, both $I(p,+) = I(n,+)$ and $I(p,-) = I(n,-)$ between $N = 88$ and 90 where the phase transition should occur. The position indices for intruder proton negative-parity states and for proton positive-parity states are almost the same. This means that an almost-equal number of proton negative- and positive-parity states lie close to the Fermi level, with a slight preference for the intruder states (higher position index) before the phase-transition point. Close to the phase-transition point a crossing of both indices occurs and after it, the proton intruder states are more distant from the Fermi level and, simultaneously, the proton pairing gets weaker. A similar situation occurs for Mo, except the weakening of the pairing interaction. A common feature of both regions, $N = 60$ and $N = 90$, namely, a gradual increase of $I(n,+)$ and $I(n,-)$ and a gradual decrease of $I(p,+)$ and $I(p,-)$ is more pronounced in the case of neodymium. In addition, in both regions, the intruder-neutron position index approaches its maximum for $N = 60$ and 90, respectively, indicating a maximum proximity of neutron intruder states to the Fermi level.

If we look closely at the single-quasiparticle (qp) states close to the Fermi level obtained in our SHF+BCS calculations, we can identify microscopic signatures of the CPS

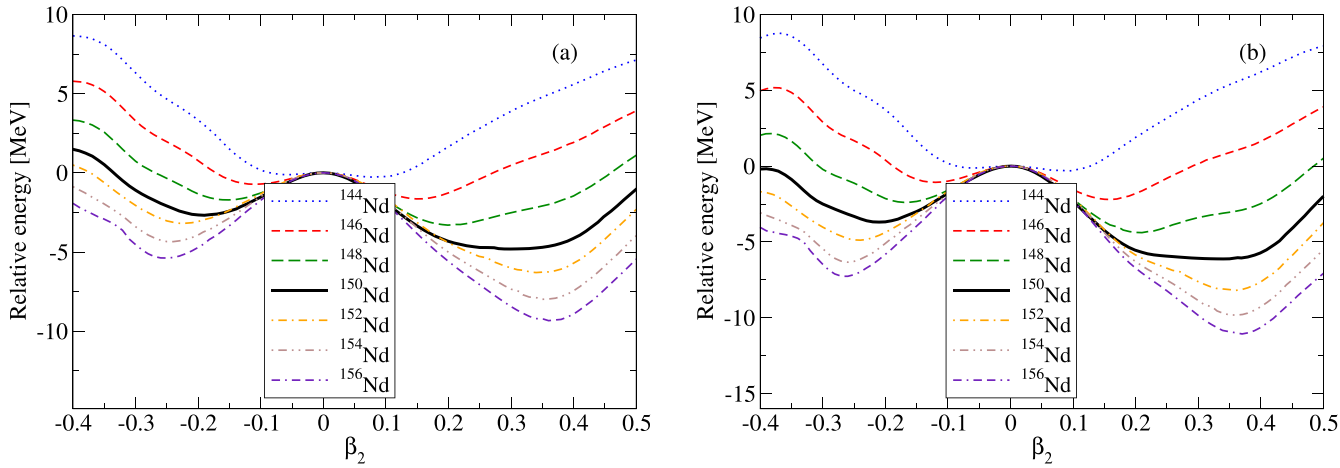


FIG. 11. PECs as a function of $\beta_2$ for the neodymium isotopes for two SHF parametrizations: (a) SV-bas and (b) SV-mas07. Flat-bottomed PECs are indicated by thicker curves.

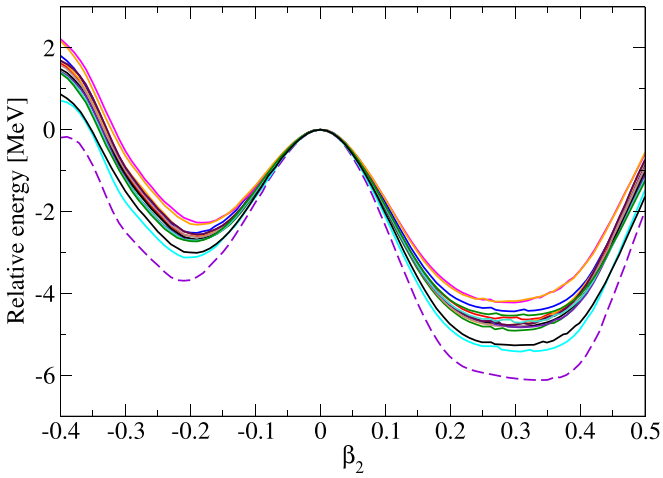


FIG. 12. PECs as a function of $\beta_2$ for $^{150}$Nd for all investigated parametrizations. The parametrization SV-mas07 (violet dashed) gives more pronounced minima.

on the single-particle level. Here, we restrict ourselves to the SV-bas parametrization only, because for other parametrizations similar results were obtained. The states resulting from the SHF+BCS calculations are characterized by the projection of the total angular momentum $j_z$ on the symmetry axis and their parity $\pi$. In Figs. 16–19 the occupation index $i = 0.5 - v^2$ for the qp states closest to the Fermi levels for the Se, Zr, Mo, and Nd chains is shown (the index $i$ approaches zero when the qp state approaches the Fermi level and is positive for particle states and negative for hole states; in addition, it approaches 0.5 for particle and $-0.5$ for hole states if the qp states are distant from the Fermi level or the pairing interaction is weak).

One can observe a typical proton-qp level crossing around the phase-transition points: in the Se chain $1/2^-$ gets occupied while $5/2^-$ is unoccupied, in the Zr and Mo chains the intruder $9/2^+$ gets occupied while $1/2^-$ is unoccupied, in the Mo chain $7/2^-$ gets occupied in addition, and in the Nd chain $3/2^+$ and the intruder $1/2^-$ get occupied while $5/2^+$ and the intruder $3/2^-$ are unoccupied and the proton pairing gets weaker.

For the Se chain and $N = 40$ the neutron pairing gets weaker, at $N = 38$ neutron-qp states $1/2^-$ and intruder $3/2^+$ cross the Fermi level and the intruder $9/2^+$ lies closer to the Fermi level and later between $N = 42$ and 44, $5/2^-$, $3/2^-$ and

TABLE II. Comparison of quadrupole deformations, $\beta_{2\text{SKYAX}}$ and $\beta_{2\text{Sky3D}}$, $\gamma_{\text{Sky3D}}$, calculated using SKYAX and SKY3D codes for the parametrization SV-bas.

| Nucleus | $\beta_{2\text{SKYAX}}$ | $\beta_{2\text{Sky3D}}$ | $\gamma_{\text{Sky3D}}$ |
|---|---|---|---|
| $^{68}$Se | −0.150 | 0.147 | 60.0 |
| $^{70}$Se | −0.126 | 0.132 | 60.0 |
| $^{72}$Se | −0.102 | 0.108 | 60.0 |
| $^{74}$Se | 0.000 | 0.000 | 22.4 |
| $^{76}$Se | 0.000 | 0.003 | 52.4 |
| $^{78}$Se | 0.053 | 0.063 | 0.1 |
| $^{80}$Se | 0.090 | 0.086 | 0.0 |
| $^{92}$Zr | 0.000 | 0.002 | 17.8 |
| $^{94}$Zr | 0.000 | 0.004 | 7.2 |
| $^{96}$Zr | 0.000 | 0.007 | 10.5 |
| $^{98}$Zr | 0.000 | 0.004 | 53.2 |
| $^{100}$Zr | −0.108 | 0.005 | 56.8 |
| $^{102}$Zr | −0.114 | 0.122 | 59.6 |
| $^{104}$Zr | −0.121 | 0.003 | 57.0 |
| $^{94}$Mo | 0.000 | 0.003 | 5.4 |
| $^{96}$Mo | 0.000 | 0.009 | 2.8 |
| $^{98}$Mo | 0.000 | 0.012 | 4.6 |
| $^{100}$Mo | 0.000 | 0.009 | 41.3 |
| $^{102}$Mo | −0.114 | 0.118 | 57.1 |
| $^{104}$Mo | −0.120 | 0.126 | 57.9 |
| $^{106}$Mo | −0.126 | 0.129 | 59.4 |
| $^{144}$Nd | 0.048 | 0.033 | 7.8 |
| $^{146}$Nd | 0.089 | 0.089 | 0.2 |
| $^{148}$Nd | 0.119 | 0.125 | 0.0 |
| $^{150}$Nd | 0.179 | 0.203 | 0.0 |
| $^{152}$Nd | 0.204 | 0.214 | 0.0 |
| $^{154}$Nd | 0.210 | 0.219 | 0.0 |
| $^{156}$Nd | 0.216 | 0.225 | 0.0 |

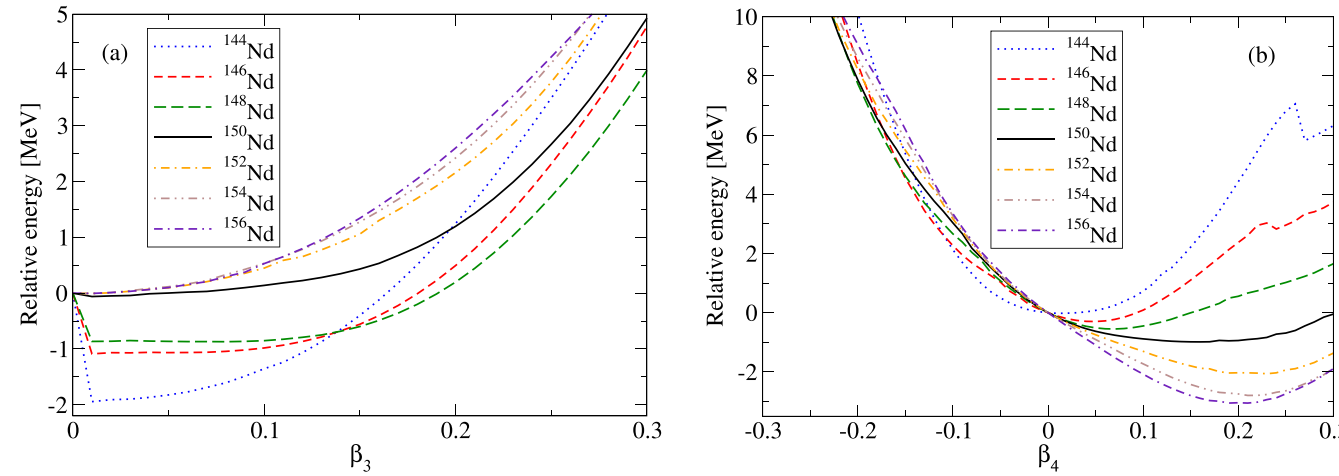


FIG. 13. PEC as a function of (a) $\beta_3$ and (b) $\beta_4$ for the neodymium isotopes for SV-bas parametrization.

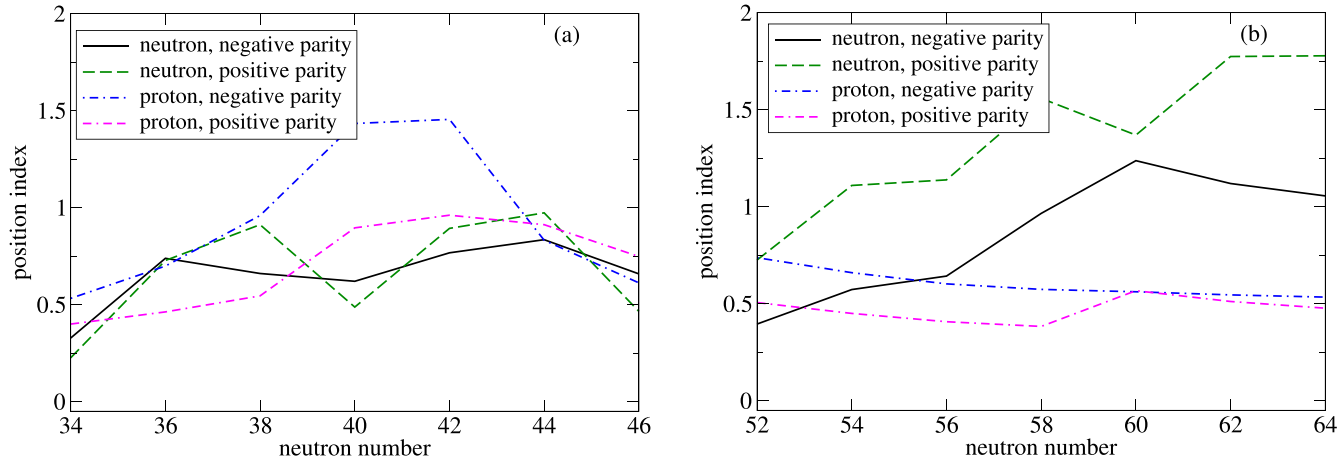


FIG. 14. Position index $I$ for the (a) selenium and (b) zirconium chains (SV-bas parametrization).

the intruder $5/2^+$ cross the Fermi level. For the Zr and Mo chains, $1/2^+$ and intruders $3/2^-$ and $7/2^-$ cross the Fermi level and become occupied, while for Mo only $5/2^+$ becomes unoccupied. In the case of the Nd chain, $3/2^-$ and the intruder $1/2^+$ get occupied around $N = 90$.

To summarize, we have found three possible microscopic signatures of criticality (QPT): (i) flatness of PECs, (ii) position index for neutron intruder states approaching a maximum value, and (iii) occupation index of selected proton qp-levels along the isotopic chain changes its sign (i.e., some particle states become hole states and v.v. at the QPT point).

To bridge from the microscopic calculations within the SHF + BCS model towards macroscopic calculations within the algebraic collective model (ACM), we can use the procedure described in Ref. [108]. In macroscopic calculations we need a potential $V_{\rm ACM}$ as a function of two deformation parameters, $\beta$ and $\gamma$. It can be constructed from the microscopic PEC as a function of $\beta_2$, $V(\beta_2)$ and expanded up to the first-order term in $\cos 3\gamma$:

$$V(\beta,\gamma) = \tfrac{1}{2}[V(\beta_2) + V(-\beta_2)] + \tfrac{1}{2}[V(\beta_2) - V(-\beta_2)]\cos 3\gamma. \quad (4)$$

The potential obtained from Eq. (4) is composed of two parts, a $\gamma$-independent symmetric part and a $\gamma$-dependent antisymmetric part. The results for the investigated $N = 40$, 60, and 90 nuclei are shown in Figs. 20 and 21 for two parametrizations, SV-bas and SV-tls. Qualitatively, we get a $\gamma$-independent well for the symmetric part of the potential and a decreasing antisymmetric $\gamma$-dependent potential for low and medium quadrupole deformations.

## IV. ALGEBRAIC COLLECTIVE MODEL

The algebraic collective model (ACM) [109–111], introduced as a computationally tractable version of the collective model of Bohr and Mottelson (BMM) [23,24] restricted to quadrupole rotational and vibrational degrees of freedom, is characterized by a well-defined algebraic structure. Unlike the conventional U(5) ⊃ SO(5) ⊃ SO(3) dynamical subgroup chain used, for example, in the Frankfurt program [112,113], as well as in the IBM [15,18], the ACM makes use of the subgroup chain [114–118]

$$\mathrm{SU(1,1)} \times \mathrm{SO(5)} \supset \mathrm{U(1)} \times \mathrm{SO(3)} \supset \mathrm{SO(2)} \quad (5)$$

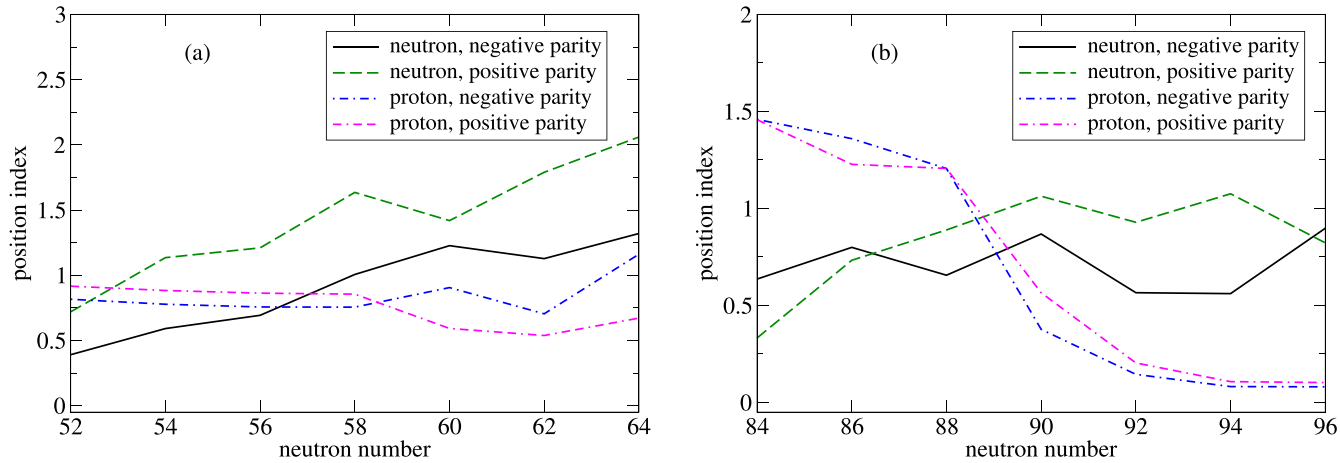


FIG. 15. Position index $I$ for the (a) molybdenum and (b) neodymium chains (SV-bas parametrization).

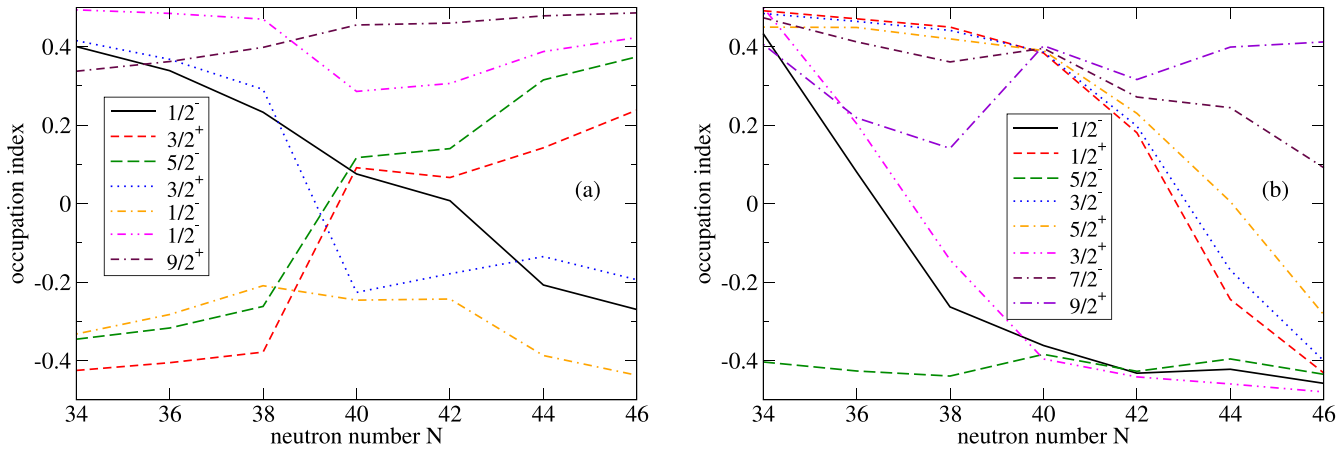


FIG. 16. Occupation index $i$ for the (a) proton and (b) neutron states closest to the Fermi level in the selenium chain (SV-bas parametrization).

to define basis wave functions as products of $\beta$ wave functions and SO(5) spherical harmonics.

Several advantages result from this choice of the dynamical subgroup chain:

(i) With the now available SO(5) Clebsch-Gordan coefficients [119,120] and explicit expressions for SO(5) reduced matrix elements, matrix elements of BMM operators can be calculated analytically [110].

(ii) By appropriate choices of SU(1,1) modified oscillator representations, the $\beta$ basis wave functions range [110] from those of the U(5) $\supset$ SO(5) harmonic vibrational model to those of the rigid $\beta$ wave function of the SO(5)-invariant model of Wilets and Jean [121].

(iii) With these SU(1,1) representations, collective model calculations converge an order of magnitude more rapidly for deformed nuclei than in U(5)$\supset$ SO(5) bases [111].

Thus, the ACM combines the advantages of the BMM and the IBM and makes collective model calculations a simple routine procedure [119,122]. A pedagogical treatment of the geometrical and algebraic foundations of the ACM can be found in the book by Rowe and Wood [123].

Recall that both E(5) [4] and X(5) [5] critical-point symmetries correspond to special solutions of the Bohr Hamiltonian [22], in which an infinite square well potential in the quadrupole ($\beta$) degree of freedom is assumed. The question of whether the assumption of a flat potential in both models is justified has been raised and investigated using various methods. Limiting ourselves to the regions of interest, we mention the following cases:

(a) The need for a potential with a nonflat bottom in $^{152}$Sm within the geometric collective model has been early realized [124]. A sextic potential possessing two minima has been used in the Bohr Hamiltonian for the description of some Nd [125], Mo [126], and Se [127] isotopes. A potential with two minima (spherical and deformed) has been recently employed in the Bohr Hamiltonian for the description of the Zr isotopes [128,129]. The existence of a bump in the PES of

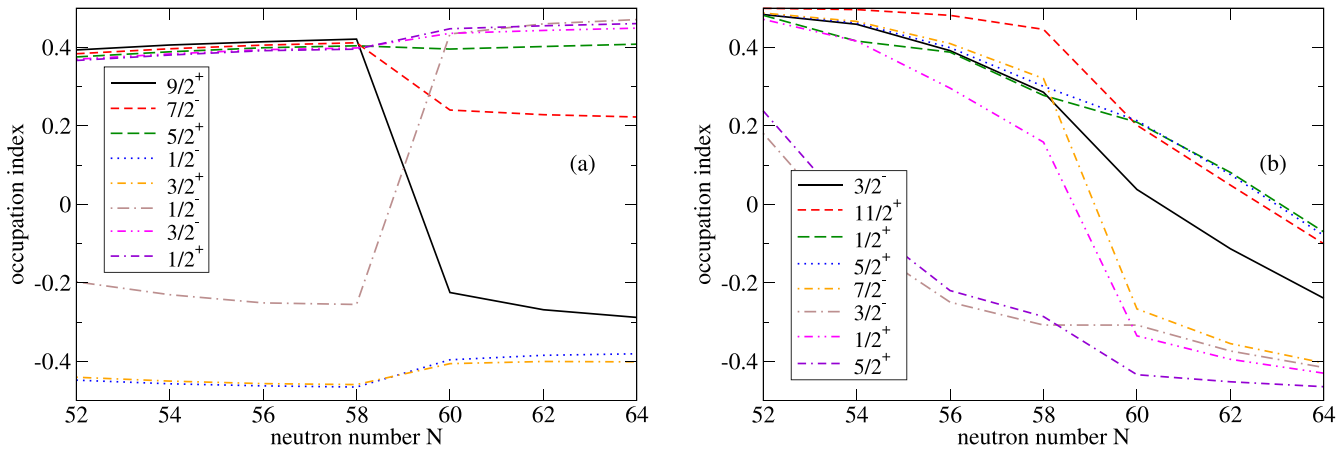


FIG. 17. Occupation index $i$ for the (a) proton and (b) neutron states closest to the Fermi level in the zirconium chain (SV-bas parametrization).

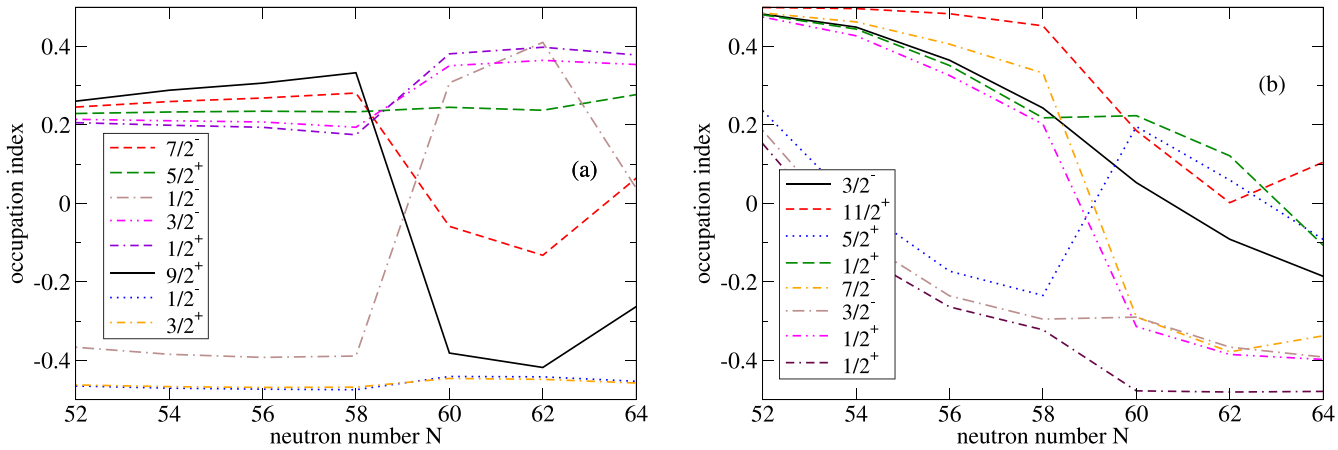


FIG. 18. Occupation index $i$ for the (a) proton and (b) neutron states closest to the Fermi level in the molybdenum chain (SV-bas parametrization).

good experimental X(5) cases might be related to the confined $\beta$-soft (CBS) rotor model [130], employing an infinite square well potential displaced from zero, as well as to the relevance of the Davidson potential $\beta^2 + \beta_0^4/\beta^2$ [131,132], where $\beta_0$ is the minimum of the potential.

(b) Potential-energy surfaces (PES) for the $N = 90$ isotones calculated in the relativistic mean field (RMF) framework [97,98] also exhibit a shape with two minima. An alternative approach [99,133], allowing for efficient calculation of spectra and transition rates, is based on the use of an IBM Hamiltonian, the parameters of which are determined by fitting the IBM PES to the PES obtained from RMF calculations. The results of these studies do not predict flat potential-energy surfaces (PES) for the $N = 90$ isotones [97–100], which are the best experimental manifestations of X(5), while a similar picture occurs also in the $N = 60$ [101] and $N = 40$ [102] isotones.

(c) Shell-model calculations in the regions of interest have been rather limited because of obvious computational hurdles. However, recent calculations [134] for the Se isotopes have pointed out the importance of the tensor force [135,136] in shaping up the nuclear properties. While the central force has a minimum at zero, the tensor force possesses a minimum at a nonzero distance from the center (see Fig. 1 of Ref. [134]), its shape roughly resembling a Kratzer potential [137,138]. Monte Carlo shell-model calculations have recently reached the Zr isotopes, studying the QPT appearing in them at $N = 60$ [139,140].

From the above the importance of having a flexible potential within the ACM to address these questions becomes evident.

In our implementation of the ACM, observables of interest are formed by taking sums of products of several generating operators, that are SO(3) invariant, such as $\hat{\beta}^2$, $\hat{\beta^{-2}}$, $\beta\frac{\mathrm{d}}{\mathrm{d}\beta}$, $\Delta^2$. The Hamiltonians that can be analyzed are polynomials in these operators with coefficients that may be arbitrary real numbers or functions of the quantum numbers on which they operate.

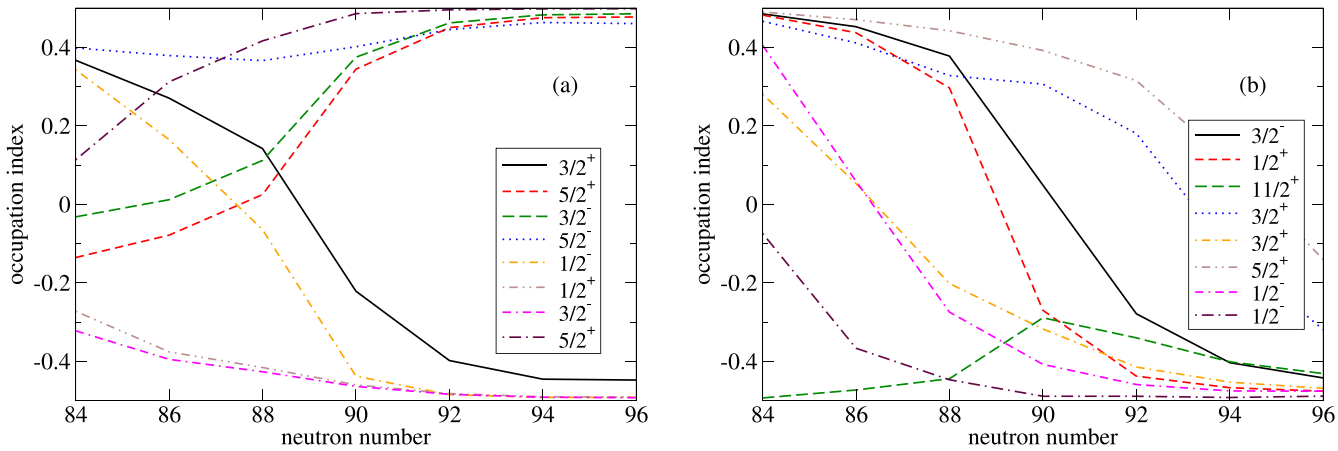


FIG. 19. Occupation index $i$ as a function of the neutron number for the (a) proton and (b) neutron states closest to the Fermi level in the neodymium chain (SV-bas parametrization).

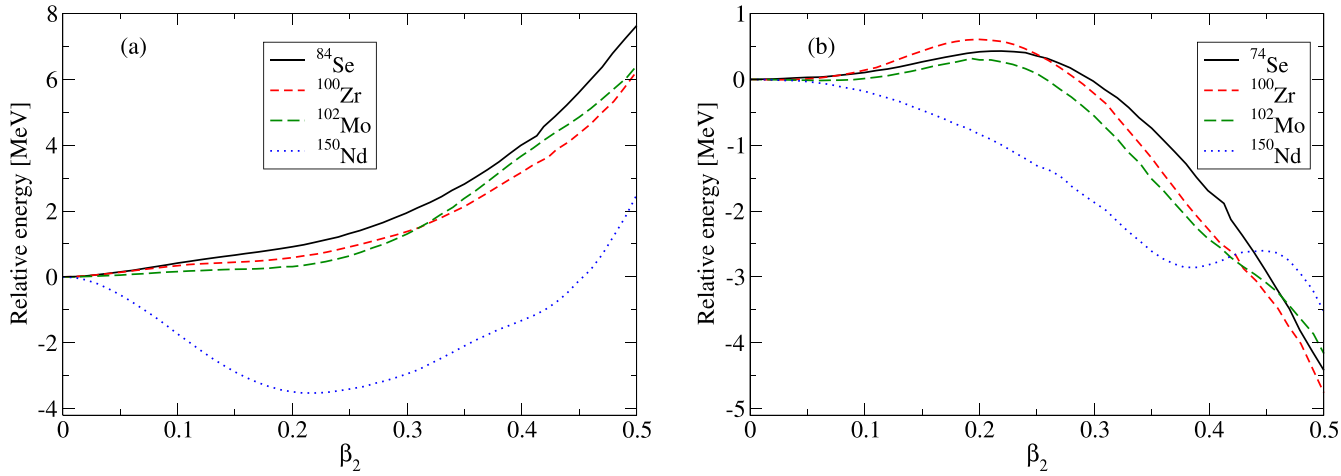


FIG. 20. (a) Symmetric and (b) antisymmetric parts of the potential derived from the microscopic PECs for the SV-bas parametrization and the investigated $N = 40$, 60, and 90 nuclei.

For the purposes of our study, the starting point will be the Hamiltonian in the form

$$\hat{H} = x_1\nabla^2 + x_2 + x_3\beta^2 + x_4\beta^4 + \frac{x_5}{\beta^2} + x_6\beta\cos 3\gamma + x_7\beta^3\cos 3\gamma + x_8\beta^5\cos 3\gamma + \frac{x_9}{\beta}\cos 3\gamma + x_{10}\cos^2 3\gamma + x_{11}\beta^2\cos^2 3\gamma + x_{12}\beta^4\cos^2 3\gamma + \frac{x_{13}}{\beta^2}\cos^2 3\gamma + \frac{x_{14}}{\hbar^2}[\hat{\pi}\otimes\hat{q}\otimes\hat{\pi}]_0, \quad (6)$$

where

$$\nabla^2 = \frac{1}{\beta^4}\frac{\partial}{\partial\beta}\beta^4\frac{\partial}{\partial\beta} + \frac{1}{\beta^2}\hat{\Lambda} \quad (7)$$

is the Laplacian on the five-dimensional collective model space and $\hat{\Lambda}$ is the SO(5) angular-momentum operator [123]. Such a Hamiltonian, expressed in terms of the quadrupole deformation parameters $\beta$ and $\gamma$ serves as a useful starting point for a description of a wide range of nuclear collective spectra. As the above Hamiltonian is a rational function of the basic observables $\hat{q}$ and $\hat{\pi}$, its matrix elements are obtained efficiently via available analytic expressions.

## V. NUMERICAL RESULTS OBTAINED WITHIN THE ALGEBRAIC COLLECTIVE MODEL

In the numerical application of the ACM to the studied nuclei we fitted the parameters of the Hamiltonian of Eq. (6) to the experimentally known low-lying members of the ground, beta, and gamma bands in $^{150}$Nd, $^{102}$Mo, and $^{74}$Se. Both theoretical and experimental spectra are shown in Figs. 22–24. As for the $^{100}$Zr, the used ACM model does not give satisfactory results. In an attempt to describe the very low energy of the $\beta$ bandhead ($R_{\beta/2_1} = 1.56$), the structure of the ground and excited bands is severely disturbed. We intend to address this issue in our future studies.

When fitting the experimental spectra, we take into account the fact that the first excited $K = 0$ state band is not necessarily the $\beta$ band [77]. There are still many questions

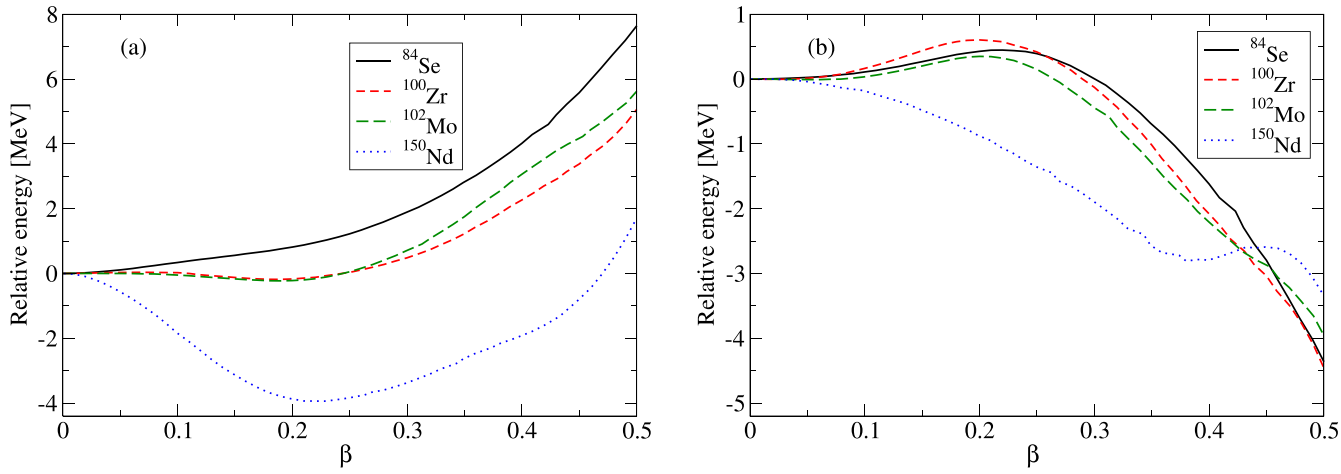


FIG. 21. (a) Symmetric and (b) antisymmetric parts of the potential derived from the microscopic PECs for the SV-tls parametrization and the investigated $N = 40$, 60, and 90 nuclei.

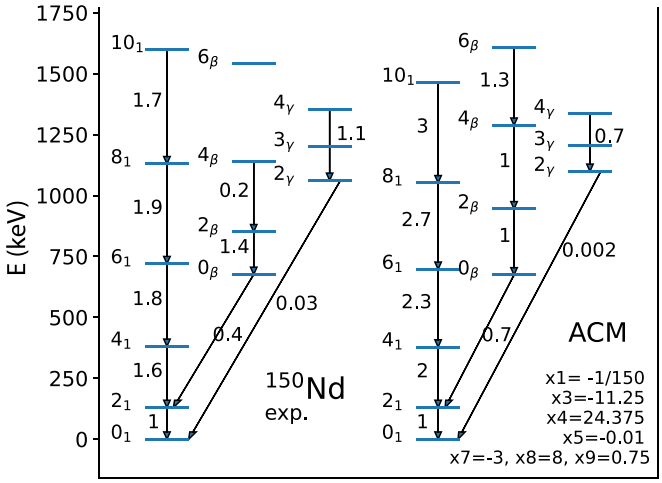


FIG. 22. Comparison of experimental (left) and ACM (right) spectra for $^{150}$Nd. The energy difference between the $2_1^+$ and $0_1^+$ states is normalized to the experimental value in $^{150}$Nd. The $B(E2)$ transition rates are expressed in units of the $B(E2, 2_1^+ \to 0_1^+) = 1$ transition. The parameters used in the ACM calculations are displayed in the right corner.

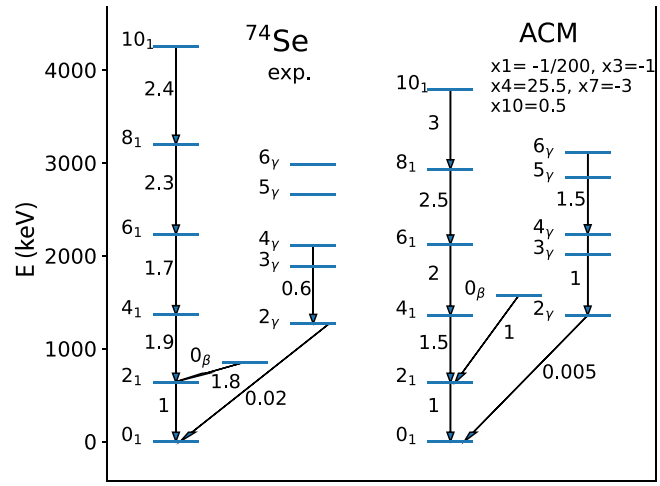


FIG. 24. Comparison of experimental (left) and ACM (right) spectra for $^{74}$Se. The energy difference of the $2_1^+$ and $0_1^+$ states is normalized to the experimental value in $^{74}$Se. The $B(E2)$ transition rates are expressed in units of the $B(E2, 2_1^+ \to 0_1^+) = 1$ transition. The parameters used in the ACM calculations are displayed in the right corner.

about the true nature of this state [73–76]. Thus, we focus the comparison to the ground-state band and to the first-excited $2^+$ states, which are undoubtedly the $\gamma$ bandheads. In doing so, we try to achieve the best possible description of the energy of the first-excited $K = 0$ state, whose low energy is a signature of the shape phase coexistence, but it is challenging, especially in case of $^{74}$Se. As a result of the attempt to describe the low-lying $K = 0$ states we observe centrifugal stretching in the ground band, all the more prominent when the energy of the first-excited $K = 0$ state decreases.

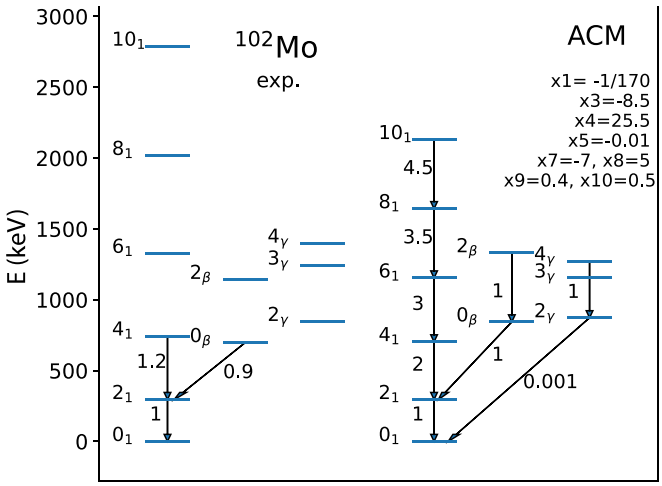


FIG. 23. Comparison of experimental (left) and ACM (right) spectra for $^{102}$Mo. The energy difference of the $2_1^+$ and $0_1^+$ states is normalized to the experimental value in $^{102}$Mo. The $B(E2)$ transition rates are expressed in units of the $B(E2, 2_1^+ \to 0_1^+) = 1$ transition. The parameters used in the ACM calculations are displayed in the right corner.

Even if the three nuclei are candidates for critical-point nuclei of a first-order QPT, we have already emphasized that the energy conditions in them are very different. For example, the ratio $R_{42}$ decreases from 2.93 in $^{150}$Nd to 2.51 in $^{102}$Mo and 2.15 in $^{74}$Se. This is very strongly reflected by the value of the parameter $x_3$, which increases from $^{150}$Nd to $^{74}$Se.

For $^{150}$Nd the agreement of the experimental and theoretical spectrum is very good. Along with the energies, the moments of inertia of the bands are also relatively well described. The $\beta$ bandhead is significantly lower than the $\gamma$ bandhead, but relatively high compared with the other two studied nuclei, the ratio $R_{\beta 2} = E(0_2)/E(2_1)$ being 5.2. Obtaining a low-lying $\beta$ band is generally a big problem mainly for lighter nuclei but in this case the energies of both $\beta$ and $\gamma$ bandheads are well fitted by the model. We also see that the ratio $B(E2, 0_2^+ \to 2_1^+)/B(E2, 2_1^+ \to 0_1^+)$ is 0.7 to be compared with the experimental value of 0.37. A big value of this ratio (above 0.3) is believed to be a signature of the QPT.

In case of $^{102}$Mo the ratio $R_{\beta 2} = E(0_2)/E(2_1)$ is about 2.4. In an attempt to fit such a low-lying state a pronounced centrifugal stretching in the ground-state band is hard to avoid. The ratio $B(E2, 0_2^+ \to 2_1^+)/B(E2, 2_1^+ \to 0_1^+) = 1$ is in an excellent agreement with the experimental value of 0.95.

$^{74}$Se is the lightest studied isotope with $R_{42}$ having a near-vibrational value of 2.15. Thus to get an overall good agreement with the experimental spectrum a higher value of the parameter $x_3 = -1$ is needed. Some centrifugal stretching is again observed in the ground band, but the energies and moments of inertia of the $\gamma$ band are very good. The energy of the $\beta$ bandhead is less satisfactory, being about twice as high as its experimental counterpart. Consequently, the theoretical ratio $B(E2, 0_2^+ \to 2_1^+)/B(E2, 2_1^+ \to 0_1^+) = 1$ is much smaller than the experimental value of seven.

Let us comment briefly on some of the parameters used in the calculation. All in all, the parameters $x_5$ and $x_8$ allow

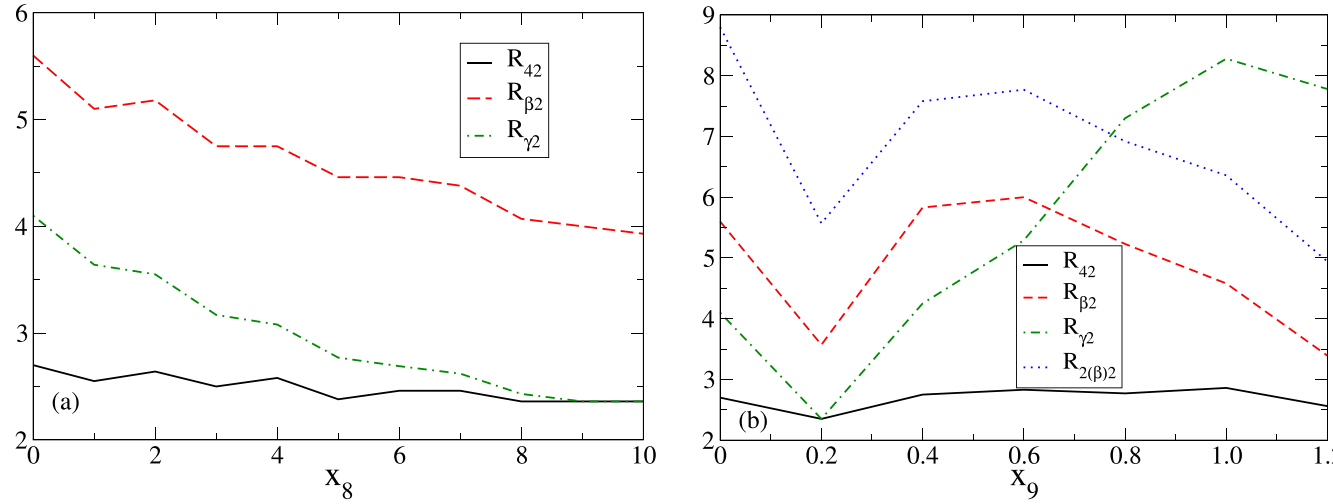


FIG. 25. Ratios $R_{42}$, $R_{\beta 2}$, and $R_{\gamma 2}$ as functions of (a) the ACM parameter $x_8$ and (b) ratios $R_{42}$, $R_{\beta 2}$, $R_{\gamma 2}$, and $R_{2(\beta)2}$ as functions of the ACM parameter $x_9$.

us to reduce the ratios $R_{42}$, $R_{\beta 2}$, $R_{\gamma 2} = E(2_\gamma)/E(2_1)$, and $R_{2(\beta)2} = E(2_\beta)/E(2_1)$, the effect of the parameter $x_8$ being more important (see Fig. 25). We may also notice that while in $^{150}$Nd the $2^+$ member of the $\gamma$ band is the third excited $2^+$ state, the situation changes in $^{102}$Mo where the $2^+$ member of the $\gamma$ band is the second excited $2^+$ state. [The second or third excited $2^+$ state is identified as a $\gamma$ bandhead based on the basis of a stronger $B(E2, 3_1^+ \to 2_{2,3}^+)$ transition]. The relative position of the $2_\gamma$ and $2_\beta$ states is strongly sensitive to the parameter $x_9$, as illustrated in Fig. 25. It can be seen that, from a certain value of this parameter, the relative position of the $2_\gamma$ and $2_\beta$ states changes. Therefore, the largest value of $x_9$ for $^{150}$Nd (among the three studied cases) is obvious. It should be noted that the term proportional to parameter $x_{10}$ in

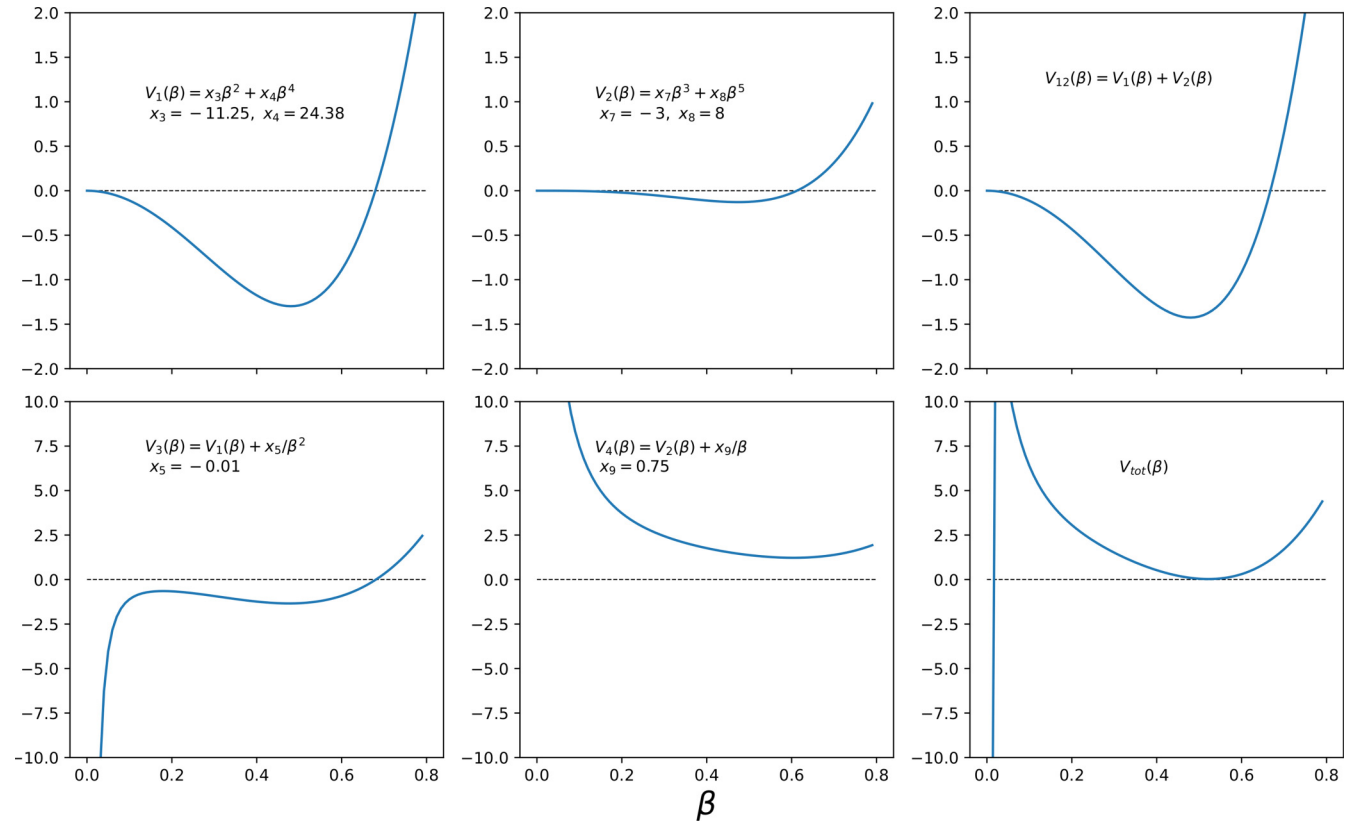


FIG. 26. Symmetric (left) and antisymmetric (middle) parts of the ACM potential and the total ACM potential (right) obtained from the fit to the experimental spectra of $^{150}$Nd. Potential terms diverging for $\beta = 0$ are excluded in the upper panel and included in the lower panel.

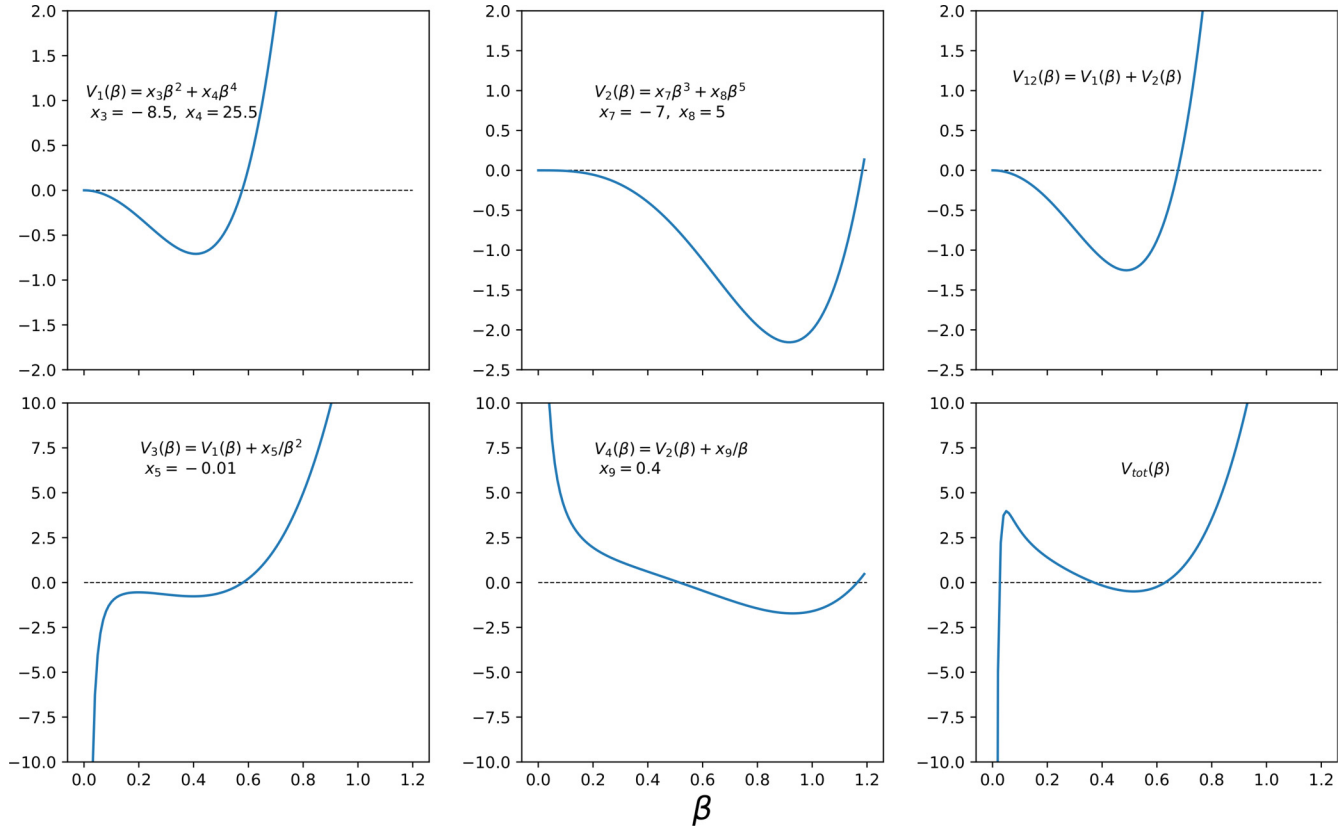


FIG. 27. Symmetric (left) and antisymmetric (middle) parts of the ACM potential and the total ACM potential (right) obtained from the fit to the experimental spectra of $^{102}$Mo. Potential terms diverging for $\beta = 0$ are excluded in the upper panel and included in the lower panel.

Hamiltonian of Eq. (6) can induce triaxiality. This term is not needed for $^{150}$Nd, where microscopic calculations result in an effective $\gamma$ value of 0° (see Table II). In the case of $^{102}$Mo and $^{74}$Se, a small parameter value of $x_{10} = 0.5$ leads to an overall improvement of the fit of the experimental spectra. This seems to be consistent with microscopic calculations, where, especially in the case of $^{74}$Se, the effective value of the parameter $\gamma = 22°$.

In Figs. 26–28 potentials used in the ACM fits for $^{150}$Nd, $^{102}$Mo, and $^{74}$Se are plotted. Their similarity to the microscopic symmetric and antisymmetric potentials (Figs. 20 and 21) for low and medium quadrupole deformation values is clearly visible, especially for $^{74}$Se and $^{102}$Mo, where the symmetric parts $V_1(\beta)$ exhibit a minimum at low or medium deformations while the antisymmetric parts $V_2(\beta)$ are decreasing. The potentials presented for $^{102}$Mo and $^{74}$Se are shown without the term $x_{10}\cos^2 3\gamma$ in Eq. (6) for simplicity, and thus under the assumption of zero triaxiality. The cases of $^{150}$Nd and $^{102}$Mo are qualitatively very similar. The upper-left panel (the symmetric potential part not depending on $\cos 3\gamma$ and

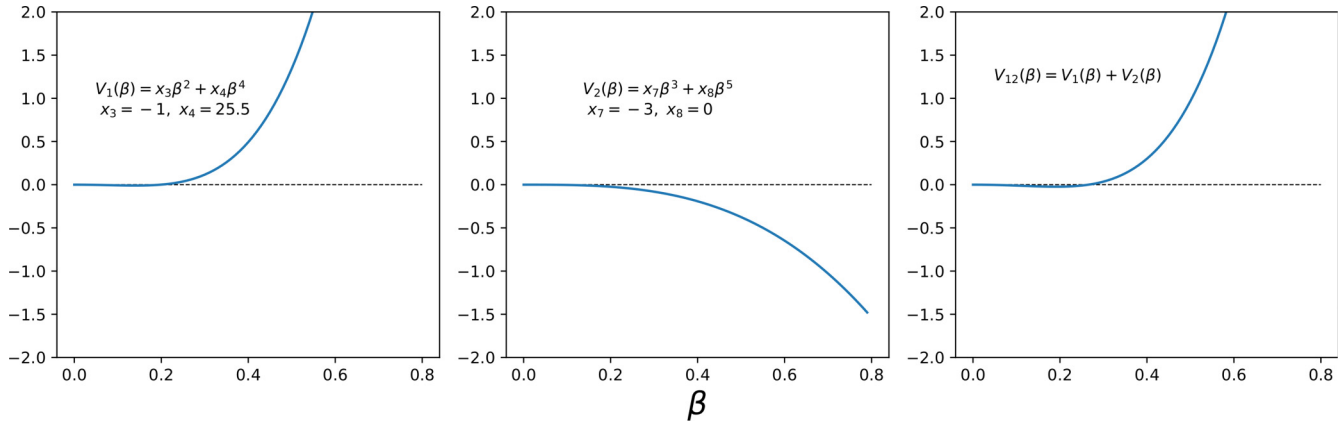


FIG. 28. Symmetric (left) and antisymmetric (middle) parts of the ACM potential and the total ACM potential (right) obtained from the fit to the experimental spectra of $^{74}$Se.

containing positive even powers of $\beta$) looks like a Davidson potential, widely used in the context of QPTs [132], except that it does not go to infinity at the origin. The upper middle panel (the antisymmetric potential part that is $\cos 3\gamma$ dependent and contains positive odd powers of $\beta$) again looks like a Davidson potential. Their sum (upper-right panel) indicates that the result is dominated by the even powers. In the lower-left and middle panels we see that the negative even powers of $\beta$ lead to minus infinity at the origin, while the negative odd powers lead to plus infinity at the origin. The final result (lower-right panel) indicates that the negative even powers dominate at the origin, but the negative odd powers dominate a little further to the right. It is clear that it is shaped up by the Davidson potential of the positive even powers, the minus infinity potential contributed by the negative even powers near the origin, and the plus infinity potential contributed by the negative odd powers a little further to the right. The final result resembles very much the confined beta-soft (CBS) model of Pietralla *et al.*, which uses an infinite square well potential displaced from the origin. This has been used for both deformed nuclei [130] and gamma-soft nuclei [70]. In other words, the main contribution of the negative odd powers is to produce the displacement from the origin.

In the case of $^{74}$Se it seems that the negative powers are not needed, since no displacement from the origin seems to be required. The total potential is dominated by the positive even powers of $\beta$. A Davidson potential is created by the positive even powers, but it is very shallow and looks flat. The same holds for the total potential. Thus in the case of $^{74}$Se the total potential looks very similar to the square well potential starting from the origin, which is used in the E(5) and X(5) CPS. The only difference is that the right wall of the potential does not rise abruptly to infinity but rises more smoothly, resembling the sloped wall potential used by Caprio [141] in the E(5) and X(5) frameworks. The main effect of the sloped wall is that it allows the beta band to go lower in energy. It also allows for $R_{4/2}$ ratios lower than the 2.91 value predicted by X(5). For example, in Fig. 6 of Ref. [141] one can see that the spectra and $B(E2)$s for $^{150}$Nd are well reproduced by a sloped well which has $R_{4/2} = 2.667$ (see also Fig. 5 of Ref. [141] for sloped wall results producing $R_{4/2} = 2.643$). However, $^{74}$Se has the experimental value of $R_{4/2} = 2.148$, thus this sloped wall alone cannot describe it.

## VI. CONCLUSIONS

In the present investigation three regions of the nuclear chart ($N = 40$, 60, 90), in which a QPT from spherical to deformed nuclei is observed, are studied on equal footing in three different ways: (a) by consideration of the empirical systematics of spectra and $B(E2)$ transition rates, (b) through microscopic mean-field calculations using the Skyrme-Hartree-Fock+BCS approach, and (c) in the framework of the Bohr Hamiltonian, using the algebraic collective model. Several similarities and differences among these three regions are pointed out.

The empirical systematics of spectra and $B(E2)$ transition rates indicate the uniform occurrence of a first-order QPT in all three regions. In contrast, they also show that the numerical values of the various indicators of collectivity differ in the three regions, showing values corresponding to high deformation at $N = 90$, intermediate deformation at $N = 60$, and low deformation at $N = 40$. From this point of view, the $N = 90$ QPT appears to be close to the parameter-independent predictions given by the X(5) critical-point symmetry, while the $N = 40$ region appears to be closer to the X(3) CPS.

The potential-energy curves obtained through microscopic Skyrme-Hartree-Fock+BCS calculations for several different parametrizations provide a flat-bottomed potential at nonzero prolate deformation in the $N = 90$ region, while in the $N = 60$ region some degree of flatness is obtained on the oblate side. In the $N = 40$ region signs of flatness appear around zero deformation.

In the framework of the algebraic collective model, the free parameters in front of the various terms in the Bohr Hamiltonian are fitted to the data. The resulting potential-energy curves in the $N = 90$ and $N = 60$ regions resemble a Davidson potential possessing a deformed minimum, being at the same time displaced from the origin, in analogy to the confined $\beta$-soft (CBS) model, applicable in deformed and transitional nuclei. In contrast, the PEC obtained in the $N = 40$ region resembles a flat potential starting from the origin, as expected within the E(5) and X(5) CPSs, albeit with a sloped right wall instead of a vertical one. The radically different picture obtained for $N = 40$ can be attributed to the fact that valence protons and neutrons in this case occupy the same major shell.

Several open questions call for further investigations. It has been shown that the symmetric and antisymmetric parts of the microscopic PECs and the ACM potential behave in a similar way at least for low and middle $\beta_2$ values. To establish a closer link between these two approaches one has to take into account also vibrational and rotational zero-point corrections in the PEC calculations and include higher-order terms in $\beta_2$ and $\cos 3\gamma$ to obtain a more realistic ACM potential. The rigid kinetic term in the ACM Hamiltonian should be also replaced by a deformation dependent ($\beta_2$ and $\cos 3\gamma$) term derived from the microscopic mass tensor that might solve the problem of rotational band stretching in $^{100}$Zr.

The preference for prolate shapes in the $N = 90$ region and for oblate shapes in the $N = 60$ region should be further investigated. Since spectra alone do not provide differentiation between prolate and oblate shapes, relevant investigations should be focused on the determination of the sign of the relevant quadrupole moments, which is opposite for oblate nuclei in relation to prolate nuclei. In light and medium-mass nuclei, in which the valence protons and neutrons occupy the same major shell, the influence of the SU(4) Wigner supermultiplet symmetry should be taken into account [142].

## ACKNOWLEDGMENTS

This work was supported by the projects SP2023/25 and SP2024/016 financed by the Czech Ministry of Education, Youth and Sports and by the GAČR Grant No. 22-14497S.

[1] R. F. Casten, Quantum phase transitions and structural evolution in nuclei, Prog. Part. Nucl. Phys. **62**, 183 (2009).

[2] P. Cejnar and J. Jolie, Quantum phase transitions in the interacting boson model, Prog. Part. Nucl. Phys. **62**, 210 (2009).

[3] P. Cejnar, J. Jolie, and R. F. Casten, Quantum phase transitions in the shapes of atomic nuclei, Rev. Mod. Phys. **82**, 2155 (2010).

[4] F. Iachello, Dynamic symmetries at the critical point, Phys. Rev. Lett. **85**, 3580 (2000).

[5] F. Iachello, Analytic description of critical point nuclei in a spherical-axially deformed shape phase transition, Phys. Rev. Lett. **87**, 052502 (2001).

[6] R. F. Casten, Shape phase transitions and critical-point phenomena in atomic nuclei, Nat. Phys. **2**, 811 (2006).

[7] R. F. Casten and E. A. McCutchan, Quantum phase transitions and structural evolution in nuclei, J. Phys. G **34**, R285 (2007).

[8] R. F. Casten and N. V. Zamfir, Empirical realization of a critical point description in atomic nuclei, Phys. Rev. Lett. **87**, 052503 (2001).

[9] R. F. Casten, D. Kusnezov, and N. V. Zamfir, Phase transitions in finite nuclei and the integer nucleon number problem, Phys. Rev. Lett. **82**, 5000 (1999).

[10] V. Werner, P. von Brentano, R. F. Casten, and J. Jolie, Singular character of critical points in nuclei, Phys. Lett. B **527**, 55 (2002).

[11] F. Iachello and N. V. Zamfir. Quantum phase transitions in mesoscopic systems, Phys. Rev. Lett. **92**, 212501 (2004).

[12] F. Iachello, Quantum phase transitions in mesoscopic systems, Int. J. Mod. Phys. B **20**, 2687 (2006).

[13] D. Bonatsos, E. A. McCutchan, R. F. Casten, and R. J. Casperson, Simple empirical order parameter for a first-order quantum phase transition in atomic nuclei, Phys. Rev. Lett. **100**, 142501 (2008).

[14] D. H. Feng, R. Gilmore, and S. R. Deans, Phase transitions and the geometric properties of the interacting boson model, Phys. Rev. C **23**, 1254 (1981).

[15] A. Arima and F. Iachello, Interacting boson model of collective states I. The vibrational limit, Ann. Phys. (NY) **99**, 253 (1976).

[16] A. Arima and F. Iachello, Interacting boson model of collective nuclear states II. The rotational limit, Ann. Phys. (NY) **111**, 201 (1978).

[17] A. Arima and F. Iachello, Interacting boson model of collective nuclear states IV. The O(6) limit, Ann. Phys. (NY) **123**, 468 (1979).

[18] F. Iachello and A. Arima, *The Interacting Boson Model* (Cambridge University Press, Cambridge, 1987).

[19] M. A. Caprio and F. Iachello, Analytic descriptions for transitional nuclei near the critical point, Nucl. Phys. A **781**, 26 (2007).

[20] R. Bijker, R. F. Casten, N. V. Zamfir, and E. A. McCutchan, Test of X(5) for the $\gamma$ degree of freedom, Phys. Rev. C **68**, 064304 (2003); **69**, 059901(E) (2004).

[21] M. A. Caprio, Effects of $\beta$-$\gamma$ coupling in transitional nuclei and the validity of the approximate separation of variables, Phys. Rev. C **72**, 054323 (2005).

[22] A. Bohr, The coupling of nuclear surface oscillations to the motion of individual nucleons, Dan. Mat. Fys. Medd. **26**, 1 (1952).

[23] A. Bohr and B. R. Mottelson, *Nuclear Structure Vol. I: Single-Particle Motion* (World Scientific, Singapore, 1998).

[24] A. Bohr and B. R. Mottelson, *Nuclear Structure Vol. II: Nuclear Deformations* (World Scientific, Singapore, 1998).

[25] R. Krücken, B. Albanna, C. Bialik, R. F. Casten, J. R. Cooper, A. Dewald, N. V. Zamfir, C. J. Barton, C. W. Beausang, M. A. Caprio, A. A. Hecht, T. Klug, J. R. Novak, N. Pietralla, and P. von Brentano, $B(E2)$ values in $^{150}$Nd and the critical point symmetry X(5), Phys. Rev. Lett. **88**, 232501 (2002).

[26] D. Tonev, A. Dewald, T. Klug, P. Petkov, J. Jolie, A. Fitzler, O. Möller, S. Heinze, P. von Brentano, and R. F. Casten, Transition probabilities in $^{154}$Gd: Evidence for X(5) critical point symmetry, Phys. Rev. C **69**, 034334 (2004).

[27] M. A. Caprio, N. V. Zamfir, R. F. Casten, C. J. Barton, C. W. Beausang, J. R. Cooper, A. A. Hecht, R. Krücken, H. Newman, J. R. Novak, N. Pietralla, A. Wolf, and K. E. Zyromski, Low-spin structure of $^{156}$Dy through $\gamma$-ray spectroscopy, Phys. Rev. C **66**, 054310 (2002).

[28] D. Bonatsos, D. Lenis, D. Petrellis, P. A. Terziev, and I. Yigitoglu, X(3): an exactly separable $\gamma$-rigid version of the X(5) critical point symmetry, Phys. Lett. B **632**, 238 (2006).

[29] P. Federman and S. Pittel, Towards a unified microscopic description of nuclear deformation, Phys. Lett. B **69**, 385 (1977).

[30] P. Federman and S. Pittel, Hartree-Fock-Bogolyubov study of deformation in the Zr-Mo region, Phys. Lett. B **77**, 29 (1978).

[31] P. Federman, S. Pittel, and R. Campos, Microscopic study of the shape transition in the zirconium isotopes, Phys. Lett. B **82**, 9 (1979).

[32] P. Federman and S. Pittel, Unified shell-model description of nuclear deformation, Phys. Rev. C **20**, 820 (1979).

[33] D. J. Rowe, Quasidynamical symmetry in an interacting boson model phase transition, Phys. Rev. Lett. **93**, 122502 (2004).

[34] G. Rosensteel and D. J. Rowe, Phase transitions and quasidynamical symmetry in nuclear collective models, III: The U(5) to SU(3) phase transition in the IBM, Nucl. Phys. A **759**, 92 (2005).

[35] D. J. Rowe, Phase transitions and quasidynamical symmetry in nuclear collective models: I. The U(5) to O(6) phase transition in the IBM, Nucl. Phys. A **745**, 47 (2004).

[36] P. S. Turner and D. J. Rowe, Phase transitions and quasidynamical symmetry in nuclear collective models. II. The spherical vibrator to gamma-soft rotor transition in an SO(5)-invariant Bohr model, Nucl. Phys. A **756**, 333 (2005).

[37] K. Heyde, P. Van Isacker, M. Waroquier, J. L. Wood, and R. A. Meyer, Coexistence in odd-mass nuclei, Phys. Rep. **102**, 291 (1983).

[38] J. L. Wood, K. Heyde, W. Nazarewicz, M. Huyse, and P. Van Duppen, Coexistence in even-mass nuclei, Phys. Rep. **215**, 101 (1992).

[39] K. Heyde and J. L. Wood, Shape coexistence in atomic nuclei, Rev. Mod. Phys. **83**, 1467 (2011).

[40] P. E. Garrett, M. Zielińska, and E. Clément, An experimental view on shape coexistence in nuclei, Prog. Part. Nucl. Phys. **124**, 103931 (2022).

[41] D. Bonatsos, A. Martinou, S. K. Peroulis, T. J. Mertzimekis, and N. Minkov, Shape coexistence in even-even nuclei: A theoretical overview, Atoms **11**, 117 (2023).

[42] J. E. García-Ramos and K. Heyde, On the nature of the shape coexistence and the quantum phase transition phenomena: lead region and Zr isotopes, EPJ Web Conf. **178**, 05005 (2018).

[43] J. E. García-Ramos and K. Heyde, Quest of shape coexistence in Zr isotopes, Phys. Rev. C **100**, 044315 (2019).

[44] J. E. García-Ramos and K. Heyde, Subtle connection between shape coexistence and quantum phase transition: The Zr case, Phys. Rev. C **102**, 054333 (2020).

[45] E. Maya-Barbecho and J. E. García-Ramos, Shape coexistence in Sr isotopes, Phys. Rev. C **105**, 034341 (2022).

[46] C. De Coster, K. Heyde, B. Decroix, P. Van Isacker, J. Jolie, H. Lehmann, and J. L. Wood, Particle-hole excitations in the interacting boson model (I) General structure and symmetries, Nucl. Phys. A **600**, 251 (1996).

[47] H. Lehmann, J. Jolie, C. De Coster, B. Decroix, K. Heyde, and J. L. Wood, Particle-hole excitations in the interacting boson model (II): The U(5)-O(6) coupling, Nucl. Phys. A **621**, 767 (1997).

[48] C. De Coster, B. Decroix, K. Heyde, J. L. Wood, J. Jolie, and H. Lehmann, Particle-hole excitations in the interacting boson model (III): The O(6)-SU(3) coupling, Nucl. Phys. A **621**, 802 (1997).

[49] C. De Coster, B. Decroix, K. Heyde, J. Jolie, H. Lehmann, and J. L. Wood, Particle-hole excitations in the interacting boson model (IV). The U(5)-SU(3) coupling, Nucl. Phys. A **651**, 31 (1999).

[50] P. D. Duval and B. R. Barrett, Configuration mixing in the interacting boson model, Phys. Lett. B **100**, 223 (1981).

[51] P. D. Duval and B. R. Barrett, Quantitative description of configuration mixing in the interacting boson model, Nucl. Phys. A **376**, 213 (1982).

[52] F. Iachello, N. V. Zamfir, and R. F. Casten, Phase coexistence in transitional nuclei and the interacting-boson model, Phys. Rev. Lett. **81**, 1191 (1998).

[53] R. F. Casten, D. D. Warner, D. S. Brenner, and R. L. Gill, Relation between the $Z = 64$ shell closure and the onset of deformation at $N = 88$–90, Phys. Rev. Lett. **47**, 1433 (1981).

[54] N. Gavrielov, A. Leviatan, and F. Iachello, Intertwined quantum phase transitions in the Zr isotopes, Phys. Rev. C **99**, 064324 (2019).

[55] N. Gavrielov, A. Leviatan, and F. Iachello, Interplay between shape-phase transitions and shape coexistence in the Zr isotopes, Phys. Scr. **95**, 024001 (2020).

[56] N. Gavrielov, A. Leviatan, and F. Iachello, Zr isotopes as a region of intertwined quantum phase transitions, Phys. Rev. C **105**, 014305 (2022).

[57] D. Bonatsos, A. Martinou, S. Peroulis, T. Mertzimekis, and N. Minkov, Signatures for shape coexistence and shape/phase transitions in even-even nuclei, J. Phys. G **50**, 075105 (2023).

[58] A. Martinou, D. Bonatsos, T. J. Metzimekis, K. E. Karakatsanis, I. E. Assimakis, S. K. Peroulis, S. Sarantopoulou, and N. Minkov, The islands of shape coexistence within the Elliott and the proxy-SU(3) Models, Eur. Phys. J. A **57**, 84 (2021).

[59] D. Bonatsos, I. E. Assimakis, N. Minkov, A. Martinou, R. B. Cakirli, R. F. Casten, and K. Blaum, Proxy-SU(3) symmetry in heavy deformed nuclei, Phys. Rev. C **95**, 064325 (2017).

[60] D. Bonatsos, I. E. Assimakis, N. Minkov, A. Martinou, S. Sarantopoulou, R. B. Cakirli, R. F. Casten, and K. Blaum, Analytic predictions for nuclear shapes, prolate dominance, and the prolate-oblate shape transition in the proxy-SU(3) model, Phys. Rev. C **95**, 064326 (2017).

[61] D. Bonatsos, A. Martinou, S. K. Peroulis, T. J. Mertzimekis, and N. Minkov, The proxy-SU(3) symmetry in atomic nuclei, Symmetry **15**, 169 (2023).

[62] D. Bonatsos, K. E. Karakatsanis, A. Martinou, T. J. Mertzimekis, and N. Minkov, Microscopic origin of shape coexistence in the $N = 90$, $Z = 64$ region, Phys. Lett. B **829**, 137099 (2022).

[63] D. Bonatsos, K. E. Karakatsanis, A. Martinou, T. J. Mertzimekis, and N. Minkov, Islands of shape coexistence from single-particle spectra in covariant density functional theory, Phys. Rev. C **106**, 044323 (2022).

[64] R. F. Casten, *Nuclear Structure from a Simple Perspective* (Oxford University Press, Oxford, 1990).

[65] S. Raman, C. W. Nestor, and P. Tikkanen, Transition probability from the ground to the first-excited $2^+$ state of even-even nuclides, At. Data Nucl. Data Tables **78**, 1 (2001).

[66] D. Bonatsos, D. Lenis, N. Minkov, P. P. Raychev, and P. A. Terziev, Sequence of potentials lying between the U(5) and X(5) symmetries, Phys. Rev. C **69**, 014302 (2004).

[67] ENSDF database https://www.nndc.bnl.gov/ensdf.

[68] B. Pritychenko, M. Birch, B. Singh, and M. Horoi, Tables of E2 transition probabilities from the first $2^+$ states in even–even nuclei, At. Data Nucl. Data Tables **107**, 1 (2016).

[69] D. Bonatsos, I. E. Assimakis, A. Martinou, S. Sarantopoulou, S. K. Peroulis, and N. Minkov, Energy differences of ground state and $\gamma_1$ bands as a hallmark of collective behavior, Nucl. Phys. A **1009**, 122158 (2021).

[70] D. Bonatsos, D. Lenis, N. Pietralla, and P. A. Terziev, $\gamma$-soft analog of the confined $\beta$-soft rotor model, Phys. Rev. C **74**, 044306 (2006).

[71] P. G. Bizzeti and A. M. Bizzeti-Sona, Evidence of X(5) symmetry for $n_\gamma = 0$, 1, 2 bands in $^{104}$Mo, Phys. Rev. C **66**, 031301(R) (2002).

[72] C. Hutter, R. Krücken, A. Aprahamian, C. J. Barton, C. W. Beausang, M. A. Caprio, R. F. Casten, W.-T. Chou, R. M. Clark, D. Cline, J. R. Cooper, M. Cromaz, A. A. Hecht, A. O. Macchiavelli, N. Pietralla, M. Shawcross, M. A. Stoyer, C. Y. Wu, and N. V. Zamfir, $B(E2)$ values and the search for the critical point symmetry X(5) in $^{104}$Mo and $^{106}$Mo, Phys. Rev. C **67**, 054315 (2003).

[73] J. F. Sharpey-Schafer, S. M. Mullins, R. A. Bark, E. Gueorguieva, J. Kau, F. Komati, J. J. Lawrie, P. Maine, A. Minkova, S. H. T. Murray, N. J. Ncapayi, and P. Vymers, Shape transitional nuclei: What can we learn from the yrare states? or hello the double vacuum; goodbye $\beta$-vibrations!, AIP Conf. Proc. **1012**, 19 (2008).

[74] J. F. Sharpey-Schafer, R. A. Bark, S. P. Bvumbi, E. A. Lawrie, J. J. Lawrie, T. E. Madiba, S. N. T. Majola, A. Minkova, S. M. Mullins, P. Papka, D. G. Roux, and J. Timár, A double vacuum, configuration dependent pairing and lack of $\beta$-vibrations in transitional nuclei: Band structure of $N = 88$ to $N = 91$ Nuclei, Nucl. Phys. A **834**, 45c (2010).

[75] J. F. Sharpey-Schafer, S. M. Mullins, R. A. Bark, J. Kau, F. Komati, E. A. Lawrie, J. J. Lawrie, T. E. Madiba, P. Maine, A. Minkova, S. H. T. Murray, N. J. Ncapayi, and P. A. Vymers, Congruent band structures in $^{154}$Gd: Configuration-dependent pairing, a double vacuum and lack of $\beta$-vibrations, Eur. Phys. J. A **47**, 5 (2011).

[76] J. F. Sharpey-Schafer, R. A. Bark, S. P. Bvumbi, T. R. S. Dinoko, and S. N. T. Majola, Stiff deformed nuclei, configuration dependent pairing and the $\beta$ and $\gamma$ degrees of freedom, Eur. Phys. J. A **55**, 15 (2019).

[77] P. E. Garrett, Characterization of the $\beta$ vibration and $0_2^+$ states in deformed nuclei, J. Phys. G **27**, R1 (2001).

[78] R. Rodríguez-Guzmán and P. Sarriguren, E(5) and X(5) shape phase transitions within a Skyrme-Hartree-Fock+BCS approach, Phys. Rev. C **76**, 064303 (2007).
[79] J. Skalski, P.-H. Heenen, and P. Bonche, Shape coexistence and low-lying collective states in $A \approx 100$ Zr nuclei, Nucl. Phys. A **559**, 221 (1993).
[80] P.-G. Reinhard, D. J. Dean, W. Nazarewicz, J. Dobaczewski, J. A. Maruhn, and M. R. Strayer, Shape coexistence and the effective nucleon-nucleon interaction, Phys. Rev. C **60**, 014316 (1999).
[81] L. M. Robledo, R. R. Rodríguez-Guzmán, and P. Sarriguren, Evolution of nuclear shapes in medium mass isotopes from a microscopic perspective, Phys. Rev. C **78**, 034314 (2008).
[82] T. R. Rodríguez and J. L. Egido, A beyond mean field analysis of the shape transition in the neodymium isotopes, Phys. Lett. B **663**, 49 (2008).
[83] T. R. Rodríguez and J. L. Egido, Study of shape transitions in $N \sim 90$ isotopes with beyond mean field calculations, AIP Conf. Proc. **1090**, 419 (2009).
[84] T. R. Rodríguez and J. L. Egido, Multiple shape coexistence in the nucleus $^{80}$Zr, Phys. Lett. B **705**, 255 (2011).
[85] S. Péru and M. Martini, Mean field based calculations with the Gogny force: Some theoretical tools to explore the nuclear structure, Eur. Phys. J. A **50**, 88 (2014).
[86] J. Meng, W. Zhang, S. G. Zhou, H. Toki, and L. S. Geng, Shape evolution for Sm isotopes in relativistic mean-field theory, Eur. Phys. J. A **25**, 23 (2005).
[87] Z.-Q. Sheng and J.-Y. Guo, Systematic analysis of critical point nuclei in the rare-earth region with relativistic mean field theory, Mod. Phys. Lett. A **20**, 2711 (2005).
[88] T. Naz, G. H. Bhat, S. Jehangir, S. Ahmad, and J. A. Sheikh, Microscopic description of structural evolution in Pd, Xe, Ba, Nd, Sm, Gd and Dy isotopes, Nucl. Phys. A **979**, 1 (2018).
[89] H. Abusara, S. Ahmad, and S. Othman, Triaxiality softness and shape coexistence in Mo and Ru isotopes, Phys. Rev. C **95**, 054302 (2017).
[90] H. Abusara and S. Ahmad, Shape evolution in Kr, Zr, and Sr isotopic chains in covariant density functional theory, Phys. Rev. C **96**, 064303 (2017).
[91] P. Kumar, V. Thakur, S. Thakur, V. Kumar, and S. K. Dhiman, Nuclear shape evolution and shape coexistence in Zr and Mo isotopes, Eur. Phys. J. A **57**, 36 (2021).
[92] S. Thakur, P. Kumar, V. Thakur, V. Kumar, and S. K. Dhiman, Shape transitions and shell structure study in zirconium, molybdenum and ruthenium, Nucl. Phys. A **1014**, 122254 (2021).
[93] Z. P. Li, T. Nikšić, D. Vretenar, J. Meng, G. A. Lalazissis, and P. Ring, Microscopic analysis of nuclear quantum phase transitions in the $N \approx 90$ region, Phys. Rev. C **79**, 054301 (2009).
[94] Z. P. Li, T. Nikšić, and D. Vretenar, Coexistence of nuclear shapes: self-consistent mean-field and beyond, J. Phys. G **43**, 024005 (2016).
[95] S. N. T. Majola *et al.*, $\beta$ and $\gamma$ bands in $N = 88$, 90, and 92 isotones investigated with a five-dimensional collective Hamiltonian based on covariant density functional theory: Vibrations, shape coexistence, and superdeformation, Phys. Rev. C **100**, 044324 (2019).
[96] J. Xiang, Z. P. Li, Z. X. Li, J. M. Yao, and J. Meng, Covariant description of shape evolution and shape coexistence in neutron-rich nuclei at $N \approx 60$, Nucl. Phys. A **873**, 1 (2012).
[97] R. Fossion, D. Bonatsos, and G. A. Lalazissis, E(5), X(5), and prolate to oblate shape phase transitions in relativistic Hartree-Bogoliubov theory, Phys. Rev. C **73**, 044310 (2006).
[98] T. Nikšić, D. Vretenar, G. A. Lalazissis, and P. Ring, Microscopic description of nuclear quantum phase transitions, Phys. Rev. Lett. **99**, 092502 (2007).
[99] K. Nomura, N. Shimizu, and T. Otsuka, Formulating the interacting boson model by mean-field methods, Phys. Rev. C **81**, 044307 (2010).
[100] K. Nomura and Y. Zhang, Two-neutron transfer reactions and shape phase transitions in the microscopically formulated interacting boson model, Phys. Rev. C **99**, 024324 (2019).
[101] K. Nomura, R. Rodríguez-Guzmán, and L. M. Robledo, Structural evolution in $A \approx 100$ nuclei within the mapped interacting boson model based on the Gogny energy density functional, Phys. Rev. C **94**, 044314 (2016).
[102] K. Nomura, R. Rodríguez-Guzmán, L. M. Robledo, Structural evolution in germanium and selenium nuclei within the mapped interacting boson model based on the Gogny energy density functional, Phys. Rev. C **95**, 064310 (2017).
[103] M. Bender, P.-H. Heenen, and P.-G. Reinhard, Self-consistent mean-field models for nuclear structure, Rev. Mod. Phys. **75**, 121 (2003).
[104] P. Klüpfel, P.-G. Reinhard, T. J. Bürvenich, and J. A. Maruhn, Variations on a theme by Skyrme: A systematic study of adjustments of model parameters, Phys. Rev. C **79**, 034310 (2009).
[105] P.-G. Reinhard, B. Schuetrumpf, and J. A. Maruhn, The axial Hartree-Fock+BCS code SkyAx, Comput. Phys. Commun. **258**, 107603 (2021).
[106] J. Terasaki, P.-H. Heenen, H. Flocard, and P. Bonche, 3D solution of Hartree-Fock-Bogoliubov equations for drip-line nuclei, Nucl. Phys. A **600**, 371 (1996).
[107] J. A. Maruhn, P.-G. Reinhard, P. D. Stevenson, and A. S. Umar, The TDHF code Sky3D, Comput. Phys. Commun. **185**, 2195 (2014).
[108] P. Klüpfel, Skyrme's interaction beyond the mean-field: The DGCM+GOA Hamiltonian of nuclear quadrupole motion, Ph.D. thesis, University Erlangen-Nürnberg, 2008.
[109] D. J. Rowe, A computationally tractable version of the collective model, Nucl. Phys. A **735**, 372 (2004).
[110] D. J. Rowe and P. S. Turner, The algebraic collective model, Nucl. Phys. A **753**, 94 (2005).
[111] D. J. Rowe, T. A. Welsh, and M. A. Caprio, Bohr model as an algebraic collective model, Phys. Rev. C **79**, 054304 (2009).
[112] P. O. Hess, J. Maruhn, and W. Greiner, The general collective model applied to the chains of Pt, Os and W isotopes, J. Phys. G: Nucl. Phys. **7**, 737 (1981).
[113] G. Gneuss and W. Greiner, Collective potential energy surfaces and nuclear structure, Nucl. Phys. A **171**, 449 (1971).
[114] S. Szpikowski and A. Góźdź, The orthonormal basis for symmetric irreducible representations of O(5)×SU(1,1) and its application to the interacting boson model, Nucl. Phys. A **340**, 76 (1980).
[115] D. J. Rowe and C. Bahri, Rotation-vibrational spectra of diatomic molecules and nuclei with Davidson interactions, J. Phys. A: Math. Gen. **31**, 4947 (1998).

[116] D. J. Rowe, An algebraic approach to problems with polynomial Hamiltonians on Euclidean spaces, J. Phys. A: Math. Gen. **38**, 10181 (2005).
[117] S. De Baerdemacker, K. Heyde, and V. Hellemans, Quadrupole collective variables in the natural Cartan–Weyl basis, J. Phys. A: Math. Theor. **40**, 2733 (2007).
[118] S. De Baerdemacker, K. Heyde, and V. Hellemans, Spectral properties of a tractable collective Hamiltonian, Phys. Rev. C **79**, 034305 (2009).
[119] M. A. Caprio, D. J. Rowe, and T. A. Welsh, Construction of SO(5) ⊃ SO(3) spherical harmonics and Clebsch–Gordan coefficients, Comput. Phys. Commun. **180**, 1150 (2009).
[120] T. A. Welsh, now accessible from https://www.physics.utoronto.ca/site-archive/rowe/taw/acm/so5/so5_home.html (2008).
[121] L. Wilets and M. Jean, Surface oscillations in even-even nuclei, Phys. Rev. **102**, 788 (1956).
[122] T. A. Welsh and D. J. Rowe, A computer code for calculations in the algebraic collective model of the atomic nucleus, Comput. Phys. Commun. **200**, 220 (2016).
[123] D. J. Rowe and J. L. Wood, *Fundamentals of Nuclear Models: Foundation Models* (World Scientific, Singapore, 2010).
[124] J.-Y. Zhang, M. A. Caprio, N. V. Zamfir, and R. F. Casten, Phase/shape coexistence in $^{152}$Sm in the geometric collective model, Phys. Rev. C **60**, 061304(R) (1999).
[125] R. Budaca, P. Buganu, and A. I. Budaca, Bohr model description of the critical point for the first order shape phase transition, Phys. Lett. B **776**, 26 (2018).
[126] R. Budaca, A. I. Budaca, and P. Buganu, Application of the Bohr Hamiltonian with a double-well sextic potential to collective states in Mo isotopes, J. Phys. G **46**, 125102 (2019).
[127] R. Budaca, P. Buganu, and A. I. Budaca, Geometrical model description of shape coexistence in Se isotopes, Nucl. Phys. A **990**, 137 (2019).
[128] E. V. Mardyban, E. A. Kolganova, T. M. Shneidman, R. V. Jolos, and N. Pietralla, Description of the low-lying collective states of $^{96}$Zr based on the collective Bohr Hamiltonian including the triaxiality degree of freedom, Phys. Rev. C **102**, 034308 (2020).
[129] E. V. Mardyban, E. A. Kolganova, T. M. Shneidman, and R. V. Jolos, Evolution of the phenomenologically determined collective potential along the chain of Zr isotopes, Phys. Rev. C **105**, 024321 (2022).
[130] N. Pietralla and O. M. Gorbachenko, Evolution of the $\beta$ excitation in axially symmetric transitional nuclei, Phys. Rev. C **70**, 011304(R) (2004).
[131] P. M. Davidson, Eigenfunctions for calculating electronic vibrational intensities, Proc. R. Soc. London A **135**, 459 (1932).
[132] D. Bonatsos, E. A. McCutchan, N. Minkov, R. F. Casten, P. Yotov, D. Lenis, D. Petrellis, and I. Yigitoglu, Exactly separable version of the Bohr Hamiltonian with the Davidson potential, Phys. Rev. C **76**, 064312 (2007).
[133] K. Nomura, N. Shimizu, and T. Otsuka, Mean-field derivation of the interacting boson model Hamiltonian and exotic nuclei, Phys. Rev. Lett. **101**, 142501 (2008).
[134] K. Kaneko, T. Mizusaki, Y. Sun, and S. Tazaki, Systematical shell-model calculation in the pairing-plus-multipole Hamiltonian with a monopole interaction for the $pf_{5/2}g_{9/2}$ shell, Phys. Rev. C **92**, 044331 (2015).
[135] T. Otsuka, A. Gade, O. Sorlin, T. Suzuki, and Y. Utsuno, Evolution of shell structure in exotic nuclei, Rev. Mod. Phys. **92**, 015002 (2020).
[136] T. Otsuka, Emerging concepts in nuclear structure based on the shell model, Physics (Basel, Switz.) **4**, 258 (2022).
[137] A. Kratzer, Die ultraroten Rotationsspektren der Halogenwasserstoffe, Z. Phys. **3**, 289 (1920).
[138] D. Bonatsos, P. E. Georgoudis, N. Minkov, D. Petrellis, and C. Quesne, Bohr Hamiltonian with a deformation-dependent mass term for the Kratzer potential, Phys. Rev. C **88**, 034316 (2013).
[139] T. Togashi, Y. Tsunoda, T. Otsuka, and N. Shimizu, Quantum phase transition in the shape of Zr isotopes, Phys. Rev. Lett. **117**, 172502 (2016).
[140] J. A. Lay, A. Vitturi, L. Fortunato, Y. Tsunoda, T. Togashi, and T. Otsuka, Two-particle transfer processes as a signature of shape phase transition in zirconium isotopes, Phys. Lett. B **838**, 137719 (2023).
[141] M. A. Caprio, Consequences of wall stiffness for a $\beta$-soft potential, Phys. Rev. C **69**, 044307 (2004).
[142] V. K. B. Kota and R. Sahu, *Structure of Medium Mass Nuclei: Deformed Shell Model and Spin-Isospin Interacting Boson Model* (CRC Press, Boca Raton, 2017).